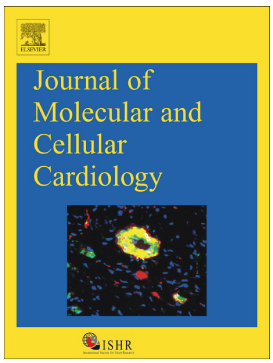

Changes in extracellular matrix in failing human non-ischemic and ischemic hearts with mechanical unloading

Yimu Zhao, Amandine Godier-Furnemont, Noortje A.M. Bax, Carlijn V.C. Bouten, Lewis M. Brown, Barry Fine, Gordana Vunjak-Novakovic

PII: S0022-2828(22)00031-1

DOI: https://doi.org/10.1016/j.yjmcc.2022.02.003

Reference: YJMCC 9485

To appear in: *Journal of Molecular and Cellular Cardiology*

Received date: 14 November 2021

Revised date: 28 January 2022

Accepted date: 11 February 2022

Please cite this article as: Y. Zhao, A. Godier-Furnemont, N.A.M. Bax, et al., Changes in extracellular matrix in failing human non-ischemic and ischemic hearts with mechanical unloading, *Journal of Molecular and Cellular Cardiology* (2021), https://doi.org/10.1016/j.yjmcc.2022.02.003

Changes in extracellular matrix in failing human non-ischemic and ischemic hearts with mechanical unloading

Yimu Zhao[1#], Amandine Godier-Furnemont[1#], Noortje A.M. Bax[2,3], Carlijn VC Bouten[2,4], Lewis M. Brown[5], Barry Fine[6], Gordana Vunjak-Novakovic[1,6]*,

[1]Department of Biomedical Engineering, Columbia University, New York, USA 10032

[2]Department of Biomedical Engineering, Eindhoven University of Technology, Eindhoven, the Netherlands

[3]Center for Care & Cure Technology Eindhoven (C3Te), Eindhoven University, Eindhoven, The Netherlands

[4]Institute for Complex Molecular Systems, Eindhoven University of Technology, Eindhoven, The Netherlands

[5]Quantitative Proteomics and Metabolomics Center, Department of Biological Sciences, Columbia University, New York, USA 10027.

[6]Department of Medicine, Columbia University, New York NY, USA 10032.

* Corresponding author: Gordana Vunjak-Novakovic gv2131@columbia.edu

[#]Yimu Zhao and Amandine Godier-Furnemont are equally contributing co-first authors.

Highlights

- Non-ischemic and ischemic myocardium display differences in the composition of extracellular matrix and respond differently to mechanical unloading by a left ventricular assist device (LVAD)
- The changes in extracellular matrix in failing hearts affect the morphology and function of human stem cell derived cardiomyocytes
- Ventricular unloading of non-ischemic hearts induces upregulation of proteins related to cardiac function
- Ventricular unloading of ischemic hearts induces upregulation of ECM proteins without reverse remodeling

Abstract

Ischemic and non-ischemic cardiomyopathies have distinct etiologies and underlying disease mechanisms, which require in-depth investigation for improved therapeutic interventions. The goal of this study was to use clinically obtained myocardium from healthy and heart failure patients, and characterize the changes in extracellular matrix (ECM) in ischemic and non-ischemic failing hearts, with and without mechanical unloading. Using tissue engineering methodologies, we also investigated how diseased human ECM, in the absence of systemic factors, can influence cardiomyocyte function. Heart tissues from heart failure patients with ischemic and non-ischemic cardiomyopathy were compared to explore differential disease phenotypes and reverse remodeling potential of left ventricular assisted device (LVAD) support at transcriptomic, proteomic and structural levels. The collected data demonstrated that the differential ECM compositions recapitulated the disease microenvironment and induced cardiomyocytes to undergo disease-like functional alterations. In addition, our study also revealed molecular profiles of non-ischemic and ischemic heart failure patients and explored the underlying mechanisms of etiology-specific impact on clinical outcome of LVAD support and tendency towards reverse remodeling.

Highlights

- Non-ischemic and ischemic myocardium display differences in the composition of extracellular matrix and respond differently to mechanical unloading by a left ventricular assist device (LVAD)
- The changes in extracellular matrix in failing hearts affect the morphology and function of human stem cell derived cardiomyocytes
- Ventricular unloading of non-ischemic hearts induces upregulation of proteins related to cardiac function
- Ventricular unloading of ischemic hearts induces upregulation of ECM proteins without reverse remodeling

Keywords

Extracellular Matrix, Heart Failure, proteomics, non-ischemic cardiomyopathy, LVAD support, ischemic cardiomyopathy, disease niches

Graphical abstract

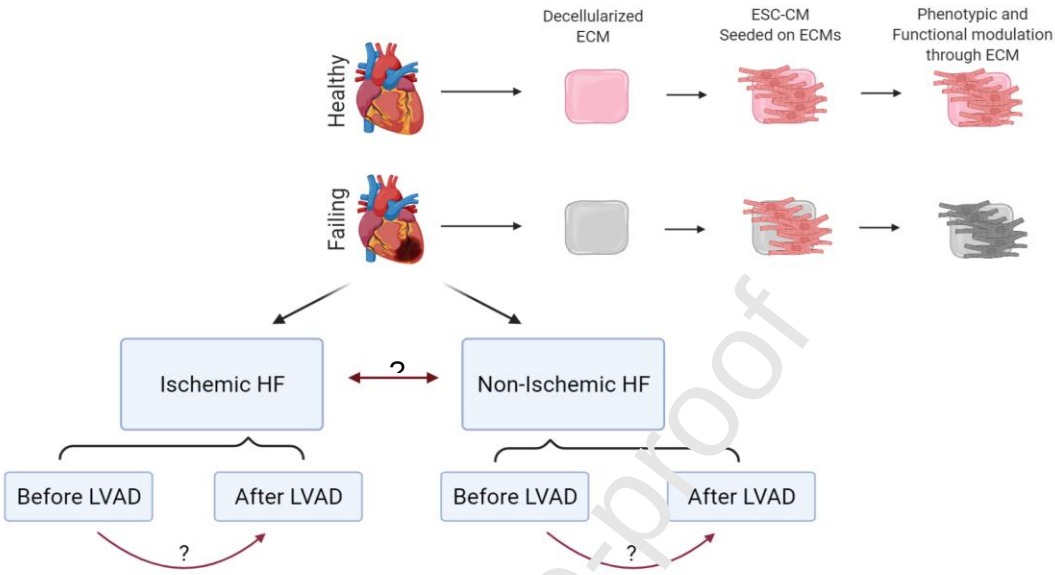

Abbreviations

APC	Activated Protein C
AR	Aspect ratio
β1AR	Adrenoreceptor beta Beta 1
bFGF	b Fibroblast Growth Factor
BMP4	Bone Morphogenetic Protein 4
BRT	Bridge to recovery
CA2	Carbonic Anhydrase
CAD	Coronary artery disease
CM	Cardiomyocytes
DKK	Dickkopf protein
EB	Embryoid Body
ECM	Extracellular Matrix
EDTA	Ethylenediaminetetraacetic Acid
CMC	Cell/Matrix Construct
ESC-EM	Embryonic Stem Cell Derived Cardiomyocyte
FDR	False Discovery Rate
F-CMC	Failing Cell/Matrix Construct
GAGs	Glycosaminoglycans
GSEA	Gene Set Enrichment Analysis
HBSS	Hank's Balanced Salt Solution
HF	Heart Failure
ICM	Ischemic Cardiomyopathy
IHC	Immunohistochemistry
LBP	Lipopolysaccharide-binding Protein
LVAD	Left Ventricular Assist Device
MI	Myocardial Infarction
MMP9	Matrix Metallopeptidase 9
MTG	Monothioglycerol
NF-CMC	Non-failing Cell/Matrix Construct

NICM	Non-Ischemic Cardiomyopathy
PCA	Principle Component Analysis
-po	Post LVAD Surgery
-pre	Pre LVAD Surgery
RNAseq	RNA Sequencing
SAA1	Serum Amyloid A
SDS	Sodium Dodecyl Sulphate
VEGF	Vascular Endothelial Growth Factor

Introduction

Heart failure (HF) is a chronic, progressive condition in which the heart muscle is unable to pump enough blood to maintain the metabolic requirements of the body. It is estimated that 6.2 million American adults were diagnosed with HF between 2013 and 2016 and, despite the research focus on early diagnosis and new therapeutic strategies, HF remains one of the most difficult diseases to treat [1].HF is generally categorized into ischemic and non-ischemic cardiomyopathy based on etiology. Ischemic cardiomyopathy (ICM) results from coronary artery disease (CAD) and myocardial infarction (MI) while non-ischemic cardiomyopathy (NICM) has a variety of etiologies including genetic, viral, toxic and idiopathic. Earlier epidemiological surveys and large-scale clinical trials suggested that the prognosis of ICM patients is worse than NICM patients [2, 3], yet the guideline-directed therapy for systolic dysfunction remains the same regardless of etiology. [4] Thus, a better understanding of disease mechanisms and etiology-specific therapeutic strategies are critical to improve patient care.

In native cardiac tissue, the extracellular matrix (ECM) is a critical component that interacts with cells and modulates tissue functions in both healthy and diseased states. ECM is a dynamic network of secreted proteins that provide structural and functional support, maintain mechanical integrity, storage and release of bioactive molecules, and serve as anchoring sites for the cells [5-8]. The heart ECM needs high compliance and stable mechanical support for the dynamic volumetric changes during contraction, which rely on the key ECM components, such as collagen, elastin and glycosaminoglycans (GAGs) [8-10]. Pressure overload induces alterations in the homeostasis of the ECM, exacerbating deterioration of cell function. ECM remodeling can dynamically adapt to stressors such as mechanical load [5] and alter its composition [11]. For example, myocardial damage resulting from external stressors leads to cardiac fibrosis, in which myofibroblasts are activated from mechanical loading [12] and deposit excessive amounts of collagen as a part of wound healing responses [13]. The altered ECMs appear different between non-ischemic cardiomyopathy (NICM), which typically has interstitial collagen deposition, and ischemic cardiomyopathy (ICM), which is more likely to have replacement fibrosis at the site of MI [14].

Decellularized tissues provide a unique opportunity to serve as cell-instructive scaffolds for engineering many tissue types, including the heart [15-18]. The first reports of decellularized hearts came in 2007 [16], followed by the use of cardiac-derived ECM in form of an entire organ, sheets and hydrogels, that were derived from rat, porcine and human hearts [19-22]. The cardiac-specific ECM was shown to be non-immunogenic and superior to collagen alone in preserving the left ventricular function [23]. Although decellularized cardiac ECM has been used to investigate its role in guiding stem cell fate [24], little is known about the regulatory roles of diseased ECM on cardiomyocytes. Thus, our study was motivated by the need to address this gap, using tissue engineering methodologies, with a focus on changes resulting from mechanical unloading. Recently, ECM-derived hydrogel was reported to preserve the biological content of ECM macromolecules, including collagen, fibronectin and laminin, in various tissue engineering applications [25]. However, the unique structure and mechanical characteristics of the diseased heart ECM are difficult to recapitulate using ECM-derived hydrogel. The use of decellularized heart sections, as in our previous studies of heart treatment by an engineered cardiac patch [26] allowed more comprehensive insights into cell-ECM interactions.

Left ventricular assist device (LVAD) is primarily used for end-stage heart failure patient to maintain their heart function while waiting for the transplantation, i.e. bridge to transplantation (BTT). In some cases, clinicians have reported myocardial recovery, in which patients have a sufficiently recovered systolic function to allow for LVAD explant instead [27-29]. During this process, LVAD support unloads the left ventricle, and this partially relaxed state of the left ventricle might result in tissue remodeling [30]. A study in 2016 reported that NICM is one of the six predictors of systolic function recovery after LVAD[29, 31]. However, the underlying mechanisms are still unclear.

The specific goal of this study was to use decellularized heart ECM from healthy and heart failure patients to explore the differences between healthy and diseased human ECM. We also used tissue engineering methodologies to investigate how diseased human ECM, in the absence of systemic environment and other signaling components (inflammation, oxygen tension), can influence the cardiomyocyte function. To this end, we studied biopsied heart tissues from heart failure patients with ischemic and non-ischemic cardiomyopathy, that underwent LVAD surgery. Whenever possible, we obtained matching tissue samples from the same patient, before and after LVAD. ECM was analyzed for the composition and morphology and used for the cultivation of human cardiomyocytes derived from stem cells. Data were analyzed and interpreted to assess differential disease phenotypes and investigate whether LVAD leads to a molecular recovery at the transcriptomic, proteomic and structural levels.

Results

Study design and patient information

We obtained left ventricular muscle samples from 20 patients with end-stage heart failure, of which 9 patients provided paired samples from LVAD surgery (NICMpre and ICMpre) and subsequent heart transplantation (NICMpo and ICMpo). Tissue samples were processed for analysis of gene expression and protein content. **Supplemental Figure 1** summarizes the patient information and the inclusion of samples in RNAseq, proteomics analysis, and histological evaluation.

All patients underwent LVAD surgery before transplantation and the average waiting period was 393 days, ranging from 102 – 1,414 days. Long-term patient tracking in this study was critical as a direct comparison of samples from before and after the LVAD procedure is particularly informative due to the high donor to donor variability. We also obtained non-failing (healthy) heart samples from healthy donors that failed to meet the transplantation screening criteria.

The experimental strategy is summarized in **Figure 1**. First, the molecular compositions of the non-failing and failing ECM were investigated by proteomic analysis. Decellularized myocardium was used as a scaffold to probe how differential molecular compositions influence the functional performance of human stem cell-derived cardiomyocytes. Then, we investigated the differences between ICM and NICM ECM at the molecular level using proteomic analysis, RNAseq, and histology. Using similar approaches, the effect of mechanical unloading on disease progression was explored for ICM and NICM ECM.

Decellularized human heart proteomics reveal differences between failing and non-failing heart

Human myocardial samples from the left ventricular apex of 3 non-failing hearts and 4 ICM hearts obtained at the time of heart transplant were used for the proteomic analysis of ECM (**Figure 2A**). The patient samples were decellularized and sectioned, as detailed in Methods (**Figure 2B**). After ECM digestion and protein purification, we performed proteomics on these samples in duplicate. Among all the detected proteins, 362 proteins were identified by more than one peptide and were used for further analysis. (**Supplemental Table 1**) Principal component analysis (PCA) of the entire proteomics data set showed a clear separation between ECM samples derived from heart failure versus healthy patients (**Figure 2C**). Differentially expressed proteins were analyzed and plotted using false discovery rate (FDR) corrected p-values and fold changes between failing and non-failing heart samples (**Figure 2D**). The most differentially expressed ECM proteins are shown in the heatmap (**Figure 2E**). Nidogen-1, thrombospondin 1 and 4, fibrillin-1, Decorin, and Emilin-1 were more abundant in non-failing heart samples, whereas multiple types of collagen proteins, versican core protein, dermatopontin and prolargin were more abundant in the failing heart samples. We confirmed the expression changes of the

four most abundant ECM proteins including vitronectin, nidogen, collagen (Picrosirius red) and laminin by histology staining (**Figure 2F**).

ECM from failing hearts creates a diseased microenvironment impairing CM function and morphology.
Because of the differential compositions of ECM proteins in the failing and non-failing heart, we explored whether ECM composition in the failing heart can act as a disease microenvironment and induce disease-like functional alterations in healthy cardiomyocytes. To this end, decellularized ECM from the failing hearts (ischemic) and healthy controls (non-failing, (NF)) were sectioned and used as a scaffold for stem cell-derived human cardiomyocytes (ESC-CM) to study the ECM-cardiomyocyte cross-talk (Figure 3A)." Previous research has documented the ability of ECM to direct ESC fate, through essential crosstalk between ESCs and ECM receptors/growth factor receptors and transduction of mechanical signals [32, 33].

The appearance of the cell/matrix construct (CMC) was documented by bright-field images in **Figure 3B.** After two weeks of culture, CMCs were tested with isoproterenol, a positive inotropic and chronotropic beta-adrenergic agonist (**Figure 3C**). The cumulative strain, measured as the summed strain rates per contractile events of EBs, was evaluated at baselined isoproterenol concentrations of 30nM, 100nM, 300nM and 1μM, where NF-CMC reached strain plateau between 300nM, and failing (F)- CMC peaked at 300nM. ECM proteins, such as elastin and fibronectin were evaluated by immunohistochemistry (IHC) to compare the CMCs from different groups (**Figure 3D**). We found reduced elastin and increased fibronectin in CMCs seeded on failing ECMs. We also investigated the expressions of cardiomyocyte proteins with immunohistology and found increased α -actinin and reduced troponin organization in F-CMCs when compared to non-failing CMC. Non-myocyte populations, stained with vimentin, were increased in F-CMCs as well. These protein expressions had consistent trend when compared to the NF and HF whole tissue proteomics.

To compare protein expressions in CMCs and corresponding patient samples, we performed whole tissue proteomics with human myocardium derived from two normal hearts and four ICM failing hearts at the time of heart transplant. Whole tissue proteomics revealed 571 proteins (**Supplemental Table 1**) with more than one peptide, and differentially expressed proteins are shown in the heatmaps (**Figure3E).** Interestingly, the expression changes of α-actinin, troponin, and vimentin from IHC on F- and NF-CMCs (**Figure 3D**) were consistent with the whole tissue proteomics performed on these patient samples (**Figure 3E**). These results suggested that ECM from heart failure patients have the altered molecular composition that may contribute to the diseased microenvironment mimicking local changes experienced by cardiomyocytes in vivo. In addition, these changes could cause disease-like functional alteration on healthy CMs.

Whole tissue proteomics and RNA-seq demonstrated different patterns between NICM and ICM patients.
In an effort to delineate the different molecular profiles between ICM and NICM failing hearts, we performed whole tissue proteomic analysis of whole tissue samples from 4 ICM patients and 4 NICM patients (**Figure 4A**). PCA showed separation between ICM and NICM patients with 61% variance for the first principal component (**Figure 4B**). Differentially expressed proteins were further analyzed and compared with non-failing samples. NICM samples had 32 differentially expressed proteins and ICM samples had 185 differentially expressed proteins, compared to non-failing samples (**Figure 4C**). All differentially expressed proteins were plotted using false discovery rate (FDR) corrected p-values and fold changes between NICM and ICM samples (**Figure 4D**).

Interestingly, the most enriched proteins in ICM, Serum Amyloid A 1 (SAA1) and Lipopolysaccharide-binding protein (LBP) are clinical biomarkers associated with coronary artery disease (CAD) [34-36]. Another highly enriched protein in ICM, activated protein C (APC), functions as a natural anticoagulant to downregulate thrombin generation in the clotting cascade, exhibiting strong cytoprotective and anti-

inflammatory activity. On the other hand, NICM enriched proteins, NDUFS7 and NDUFA6, are both proteins involved in the largest enzyme of the mitochondrial membrane respiratory chain (NADH: ubiquinone oxidoreductase complex I) [37, 38]. The enrichment of these proteins in NICM groups may suggest a higher level of mitochondria-related cellular activity.

Gene ontology term pathway analysis of differential proteomic expression demonstrated upregulation of ECM organization, contractile function and immunological responses in ICM myocardium, whereas NICM myocardium displayed upregulation of oxidoreductase activity (**Figure 4E**). In terms of differentially expressed proteins, ICM samples showed upregulation of cardiac sarcomere proteins, such as multiple myosin proteins, tropomyosin 3, cadherin 13 and actin proteins. There were also various types of collagens, collagen fragments (endostatin), β2-glycoprotein 1, and a matrix degradation protein, matrix metalloproteinase 9 (MMP9), that were upregulated in ICM samples. The elevated vimentin, a classic non-myocyte marker, indicated the increased non-myocyte population in ICM that was consistent with elevated collagen secretion. NICM samples, on the other hand, had more expressions on mitochondria-related proteins, indicating the potential higher cellular activities, such as metabolism and oxidative phosphorylation (**Figure 4F**). The Gene Set Enrichment Analysis (GSEA) of proteomics revealed similar findings, in which ICM samples had upregulation of inflammatory responses, pathways related to wound healing and phagocytosis and NICM samples had higher fatty acid oxidation and metabolic activities (**Figure 4G**).

We further compared these data with the RNAseg dataset (**Supplemental Figure 2, Supplemental Table 3**), performed on two ICM and two NICM patient samples. Although the separation between NICM and ICM samples was shown by PCA, unsupervised hierarchical clustering of samples did not correspond to the etiological differences. GSEA demonstrated enriched striated muscle contraction, cardiac contractile machinery and fibroblast development in ICM patient samples, which were consistent with proteomics data.

We also performed histology staining and quantification of samples from NICM and ICM patients (n=4 per group) to evaluate cardiac functional proteins by Troponin T and N-cadherin; extracellular collagen deposition by Picro Sirius Red and fibronectin (**Supplemental Figure 3**). When directly comparing NICMpre and ICMpre (patient samples before LVAD), ICM patients tended to have a higher expression of troponin T, better aligned N-cadherin, more collagen deposition and similar fibronectin expression compared to NICM patients (**Supplemental Figure 3**). These results were consistent with the proteomic and RNAseq analyses.

In summary, the analysis of whole tissue proteomics and RNAseq datasets and histology demonstrated upregulated inflammation responses, higher expressions of sarcomere proteins, elevated ECM protein secretion and increased non-myocyte populations in ICM samples. NICM samples showed enriched metabolic activity that related to mitochondrial function.

LVAD Attenuated NICM Disease Progression

We obtained myocardial tissues from four NICM patients during LVAD surgery (NICMpre) and after heart transplantation (NICMpo), to investigate how LVAD influenced the progression of ECM through the analysis of whole tissue proteomics (**Figure 5**) and RNAseq based gene expressions (**Supplemental Figure 4, Supplemental Table 3**). All proteins from the proteomic dataset were included for PCA and there was an incomplete separation between NICMpre and NICMpo samples (**Figure 5B**). NICMpre and NICMpo were compared to healthy donors respectively to identify their differentially expressed proteins, where NICMpo samples had 32 differential expressed proteins and NICMpre samples had 55 differential expressed proteins, compared to non-failing samples. NICMpre and NICMpo shared 17 differential expressed proteins with non-failing samples (**Figure 5C**). The reduction of differentially expressed proteins after LVAD suggested that NICMpo resembled better with non-failing samples.

We further directly compared NICMpre and NICMpo samples for differential expressed proteins, (**Figure 5D**) all of which were included in the volcano plot using FDR corrected p-values and fold changes between NICMpre and NICMpo samples. Tropomyosin 1,2 and 3 were among the most upregulated proteins in NICMpo samples. Tropomyosin is the key regulatory component of the thin filament and plays a central role in the cardiac muscle's cooperative activation mechanism [39]. Similarly, small calcium (Ca2+) -binding protein (S100A1) that was upregulated in NICMpo, is a key regulator of cardiac performance, by controlling Ca2+-influx and restoration [40, 41]. On the other hand, carbonic anhydrase 2 (CA2), showed the highest upregulation in NICMpre, is a marker for cardiac hypertrophy and ICM progression [42, 43]. Moreover, GO term pathway analysis showed upregulation of CM function-related proteins and downregulation of ECM region activity in NICMpo (**Figure 5F**). The trends of reduced collagen deposition in NICMpo histologically and the elevation of cardiac function-related pathways from GSEA were also in agreement with this finding (**Supplemental Figure 3, Figure 5G**).

The proteomics data were further confirmed by RNAseq analysis (**Supplemental Figure 4**). We included NICMpre, NICMpo and non-failing samples in the comparison. Both the PCA plots and correlation based hierarchical clustering of experimental groups demonstrated better resemblance of NICMpost myocardium with non-failing samples. When comparing between NICMpre and NICMpo, GSEA also showed depleted immune responses and mitochondria activity, more enriched sarcomere proteins and action potential related gene sets in NICMpo.

Cell-cell interaction is the key regulator of mechanical and electrical coupling between cardiomyocytes that maintains cardiac function. The intercalated disc complex located at the transverse junction between cardiomyocytes is responsible for such communication and can be significantly reduced in heart failure patients [44]. Since we found significant enrichment in cell adhesion pathways in NICMpo, adherens junction N-cadherin and gap junction connexin 43 were assessed. Consistently with pathway analysis, tissue histological staining of N-cadherin showed significantly increased expression in staining after LVAD (n=4, paired t-test, p=0.0151, **Supplemental Figure 3**), while RNA level of N-cadherin showed a trend of increase after LVAD. Cx43 staining also trended higher in NICMpo group (data not shown). GSEA from RNAseq confirmed the enrichment in cell-cell signaling and cardiac conduction (**Supplemental Figure4 and Supplemental Table 3**).

These results demonstrated that after LVAD, NICMpo samples resembled more closely the non-failing samples in terms of protein and RNA expressions. Compared to NICMpre, NICMpo exhibited enrichment of S100A1, tropomyosin, a-actinin and other cardiac functional proteins, as well as increased adheres junction protein N-cadherin. There were enriched GO term pathways in cardiac contraction and contractile machinery and reduced ECM activity in NICMpo. Also, GSEA showed enrichment of cardiac contractile proteins and reduced inflammation. All of the above data were consistently supported that the LVAD procedure attenuated the molecular markers of NICM.

Comparison of ICM patient samples before and after LVAD.

Myocardial tissues from four ICM patients during LVAD surgery (ICMpre) and after heart transplantation (ICMpo) were compared to investigate how LVAD influences the progression of ICM through the analysis of whole tissue proteomics (**Figure 6**) and RNAseq based gene expressions (**Supplemental Figure 5, Supplemental Table 3**).

PCA from whole tissue proteomics did not show a good separation between ICMpre and ICMpo samples (**Figure 6B**). When ICMpre and ICMpo were compared to non-failing samples to identify differentially expressed proteins, ICMpre and ICMpo samples had 185 and 177 differentially expressed proteins, respectively, compared to non-failing samples (**Figure 6C**). When ICMpre and ICMpo were compared for their differentially expressed proteins, volcano plot revealed the most upregulated proteins in ICMpo groups. In particular, ASPN has been demonstrated to be a potential biomarker for heart failure [45], and periostin (POSTN) that has been associated with myocardial fibrosis in human failing hearts were

highly upregulated (**Figure 6C**). A list of most differentially expressed proteins is included in the heatmap. ICMpo samples had enriched collagen proteins and immunoglobins, whereas ICMpre had higher levels of N-cadherin (cadherin 2). Both ICMpre and ICMpo samples had different types of enriched sarcomere proteins and mitochondrial membrane proteins (**Figure 6D**). GO terms pathway analysis showed upregulation of ECM organization and downregulation of mitochondria, respiration, fatty acid metabolism, CM contraction-related pathways in ICMpo samples (**Figure 6E**). GSEA of differential protein expression indicated downregulated immune response and stress-related pathways, as well as cell proliferation in ICMpo (**Figure 6F**).

For RNAseq analysis, both PCA plots and hierarchical clustering of samples were created among ICMpre, ICMpo and non-failing samples, and the three groups did not clearly separate. GSEA of RNASeq also showed enriched genes in ECM organization and collagen production, which is consistent with GO terms pathway analysis (**Supplemental Figure 5**). Based on these results, LVAD treatment did not result in significant changes in either protein or RNA expression in ICM tissues.

Discussion

Although biological specimens have been collected for use in a variety of molecular epidemiology, clinical trials and basic research studies for years, human cardiac specimens are particularly difficult to obtain due to their non-regenerative and vital nature. Nevertheless, as heart failure involves the pathological interactions among the immune system, vascular network, cardiac muscles and electrical conduction systems, the complexity of the disease requires clinical samples to investigate the entire context. On the other hand, researchers can generate in vitro cardiac tissue models such as cardiac organoids and heart-on-a-chip with the recent technological advances in in vitro culture systems and induced pluripotent stem cells [46-48]. These tissue models are very versatile tools that enable the dissection of the individual contribution of cells and matrix to the diseases in a precisely controlled and biomimicry microenvironment. Therefore, in this study, we uniquely combined both approaches to carry out an in-depth investigation of the disease mechanisms. We first obtained human healthy and heart failure samples as well as the longitudinal tissue samples across a period up to 4 years for paired before and after LVAD implantation. We identified the alteration of molecular composition from decellularized ECM as a disease niche in heart failure samples and validated it with our in vitro CMCs.

We demonstrated molecular differences between ECMs from non-failing and failing hearts, consistent with the notion that ECM is the essential part of the myocardium that interacts with cells. For example, nidogen is a basement membrane glycoprotein and the knockout studies in mice have shown to be important for cardiac tissue integrity [49]. Studies with human myocardium as well as models of pressure overload in rodents demonstrated that Nidogen is downregulated in heart failure [50], which is consistent with our findings. Similarly, thrombospondins are glycoproteins responsible for cell-cell adhesion and cell-matrix interaction, which was reported to decrease in failing hearts [51]. On the other hand, as the top upregulated ECM protein in failing samples, dermatopontin was shown to interact with other ECM components, especially decorin, to regulate ECM formation. A rodent model demonstrated an elevated mRNA level of dermatopontin after MI that was consistent with our finding [52] Similarly, prolargin protein level was also elevated in heart failure patients [53]

When culturing human cardiomyocytes on diseased ECMs, cardiac function and secreted proteins were significantly affected and became aligned with the in vivo diseased state. We found reduced elastin and increased fibronectin in CMCs seeded on failing ECMs, which were consistent with the literature. While the exact mechanisms are still under investigation, the study showed that the increase in fibronectin content after MI [54] was associated with the increased abundance of cardiac myofibroblasts (MF). Also,

fibronectin polymerization was necessary for collagen matrix deposition, and fibrosis was attenuated while inhibiting fibronectin production. [55] The reduction of elastin expression in heart failure patient samples may stem from the reduced protein expression of Emilin-1, the elastin receptor, which eventually results in the reduction of tissue compliance due to the gradual replacement of elastin with collagen content in ECM after injury [56]. Reduced cardiac functional proteins and increased non-myocyte population suggested a shift from normal to fibrosis state. The lower sensitivity of isoproterenol was also in agreement with the pathological phenotype, as a result of their cell-matrix interactions. These differential cellular performances suggest an essential regulatory role of ECM from both healthy and diseased tissues.

Compared to NICM, ICM patient samples preserved better their cardiac functional proteins, elevated ECM depositions, and had a higher level of inflammatory response than NICM patients. In ICM patients, ventricular dysfunction is a consequence of myocardial ischemia and infarction related to coronary arteriosclerosis. Because damage and remodeling are more restricted to the infarct sites, ICM are often accompanied by a higher level of immune responses, which was identified with our proteomic analysis [57]. NICM often results from pressure overload, in which the disease alteration is presented for the entire pressure baring chamber. This process relates less to immune responses and more directly to the myofibroblast activation via mechanosensing and TGF-β signaling [58].

NICM is broadly defined as cardiomyopathy without CAD, with varying etiologies. Subtypes such as hypertrophic and dilated cardiomyopathy often result from high blood pressure and chronic cardiac overload. LVAD procedure can remove the pathological trigger through mechanical unloading and facilitate cardiac recovery. This attenuation of disease phenotypes potentially through N-cadherin-dependent mechanosensing cascade [59]. In this study, the proteomic and RNAseq analysis consistently identified the gene sets and pathways related to upregulated cardiac contractile functions, signal transduction, and downregulated inflammatory responses in NICMpo. The histology staining of heart tissues from NICMpre and NICMpo confirmed the improved Troponin T expressions after the LVAD. The histology quantification also confirmed that N-cadherin was upregulated after the LVAD procedure in the NICM group.

Interestingly, ICM patients did not show the same responses. Although the inflammatory pathways are downregulated as well, while the pathways of cellular activities including metabolism, cellular respiration, muscle contraction are downregulated simultaneously. The most noticeable upregulation in ICMpo are the pathways related to the increased non-myocyte populations and ECM matrix organization, which indicates the fibroblasts were activated and scar formation was still progressive. Both Troponin T and N-cadherin demonstrated a trend of down-regulation, suggesting reduced cardiac function. It is possible that the mechanical unloading in ICM patients is interfering with the necessary mechanical stimulation required for the heart to maintain its homeostatic function [60, 61].

In a study of 15,138 patient outcomes in the INTERMACS cohort, LVAD was evaluated as a potential therapeutic strategy – bridge to recovery (BTR) instead of conventional BTT and the author constructed a recovery predictive model. NICM is one of the six independent predictors for cardiac recovery of LVAD [29]. Other studies also confirmed that positive clinical outcomes are strongly associated with NICM patients [27-29, 31]

Our findings are aligned with these studies of cardiac recovery after long-term LVAD, providing a more in-depth investigation at a molecular level to explain the etiology-specific preference of BTR therapy with LVAD. Despite the patients under current investigation being categorized in bridge to transplant group, which is not typically suitable for BTR therapy, the NICM patients still demonstrated a moderate level of functional recovery evident from the elevated cardiac function proteins. ICM patients, on the other hand, showed depletion of cardiac functional proteins, reduced levels of mitochondria-related activities, such as oxidative phosphorylation and various metabolic processes, and downregulation of

inflammatory gene sets. The reduced cardiac functions and cellular activities strongly indicated ICM patients may not benefit from the BTR therapy.

The primary limitation of this study is the small sample sizes, which were dictated by the availability of clinical samples. We only had four biological replicates for proteomics and two for RNAseq from heart failure patients to compare with 2-3 non-failing patient samples. Moreover, although both histology quantification and RNAseq data were obtained using paired patient samples before and after LVAD, we were only able to include two pairs from the same patients and two mismatched pairs for proteomic analysis. Therefore, donor variability would be a concern as well.

Intragroup variability was also observed in the non-failing group and ICMpo group (1 vs 2-4). Low sample sizes, sample mismatch, and intragroup variability can significantly reduce the power of analysis. As the intragroup variability results from donor variability, the molecular composition of non-failing and failing tissues can vary based on age, gender, environmental factors, and diseases related or unrelated to the heart [62]. Surgical harvest of heart tissue can also contribute to the intragroup variability due to the slight differences in the region of operation. Larger sample sizes would reduce the noise and to distill the critical mechanistic information, but are difficult to obtain, especially the matched samples before and after the intervention.

Despite these limitations, our histology and RNAseq experiment were performed on matched pairs which minimized the effects of donor variability. The consistency among proteome, transcriptome, and protein expressions in histological staining allowed us to reach conclusions, in spite of low sample sizes, donor variability, and sensitivity in techniques."

The LVAD effect on histological quantifications, such as cardiac fibrosis and N-cadherin, had a consistent trend in every patient before and after LVAD. Although high donor to donor variability leads to no significant differences, the strength of the analysis lies in the consecutive measurements in the same patients before and after LVAD implantation, elimination in this way variable results due to variations in patient population. This study is setting the first steps in understanding the contribution of LVAD support on cardiac recovery and therefore providing valuable information to the research field.

In conclusion, this proof-of-concept study demonstrated the impact on the ECM niche and its effect on functional alteration of cardiomyocytes towards in vivo diseased state. This study also revealed molecular profiles of NICM and ICM heart failure patients and explored the underlying mechanisms of etiology-specific impact on clinical outcome of LVAD support and tendency towards reverse remodeling.

Methods

Procurement of Patient Heart Tissues.

Myocardial tissue samples were obtained from the apical core biopsy during LVAD implantation and subsequently at the time of cardiac transplantation after LVAD-support. Detailed information is presented in **Supplemental Figure 1**. Patient consent was obtained and tissue was collected according to Columbia University's International Review Board protocol for de-identified tissue/data.

Preparation of Decellularized Scaffolds.

Sections of the human myocardium were decellularized using a modified version of a protocol we previously described [63]. At the time of sample collection, the human myocardium was flash frozen and stored at -80°C, until the time of use. Briefly, tissue samples were sectioned into 240 µm slices on a cryotome, washed in deionized water for 20 minutes, followed by 2 h of lysis in 10 mM Tris buffer and 0.1% wt/vol EDTA, followed by 6 h of solubilization in 0.5% SDS with orbital mixing. Sections were washed in PBS, incubated in PBS containing 50 U/ mL of DNase (Sigma-Aldrich) and 1 U/mL, and washed

in HBSS with orbital mixing to remove the detergent and cell debris. These sections were either used to characterize the tissue ECM or as scaffolds for the cultivation of human cardiomyocytes

Cell preparation

Cardiomyocytes were generated from human embryonic stem cell line HES2 according to a previously published protocol[64]. Briefly, embryoid bodies were formed by plating small aggregates of human ESCs in 2 ml basic media (StemPro34, Invitrogen, containing 2 mM glutamine, 4 × 10-4 M monothioglycerol (MTG), 50 µg ml-1 ascorbic acid, Sigma, and 0.5 ng ml-1 BMP4). At days 1–4, BMP4 (10 ng/ml), bFGF(5 ng/ml) and activin A (3 ng/ml) were added for primitive-streak formation; at days 4–8, VEGF(10 ng/ml) and DKK1 (150 ng/ml), were added for mesoderm induction; after day 8, VEGF (10 ng/ml), DKK1 (150 ng/ml), and bFGF (5 ng/ml) were added for cardiac specification. Cultures were maintained in a 5% CO2/5% O2/90% N2 environment for the first 10–12 days and transferred to a 5% CO2/air environment for culture maintenance.

Cell/Matrix Constructs

Decellularized human scaffolds were cut into 2 mm x 5 mm scaffolds and placed into flat-bottom, ultra-low attachment 96 well plates (Costar). On day 23, embryoid bodies from cardiac differentiation culture were dissociated using Blendzyme TM (Roche) in HBSS at 37°C for 40 minutes. The dissociated cardiomyocytes were mechanically agitated, pelleted, and resuspended in basic media [65]. Cardiomyocytes were seeded onto decellularized scaffolds using 10^5 cells per scaffold in 0.2 mL basic medium. Cells were cultured on scaffolds for 2 weeks, with medium change every other day.

Functional Analysis

On day 14, the contractile behavior of the construct was assessed by video analysis during various interventions. Tissue constructs were placed into Tyrode's solution containing 140 mM NaCl, 5.4 mM KCl, 1 mM MgCl2, 10 mM glucose, 0.4 mM $CaCl_2$ and 10 mM HEPES (pH 7.4 with NaOH at 25°C) (adapted from [66]). Under video analysis (60 fps, 10x magnification), baseline beating was recorded followed by stepwise isoproterenol stimulation from 0.01 µM to 1 µM, at 4-minute intervals. Videos were analyzed for cumulative strains of construct under isoproterenol stimulation, according to methods developed by Kamgoue et al [67, 68]. As EBs beat, grey intensity patterns were measured by the built-in cross-correlation function comparing interrogation areas between two adjacent frames, and generated velocity vectors between the areas of similar intensity. Strain rate was determined using built-in PIVlab functions of MATLAB, and compared with point-to-point contraction/relaxation data. An integral of the strain rate over the beating area was determined for each frame and averaged over the entire area of interest, resulting in a strain rate that could be traced over time. Positive strain rates for the contractile events were summed up to determine the cumulative strain, and divided by the number of contractions to determine the strain per beat.

Immunohistochemistry

For histology, pieces of native human heart tissue were fixed in 4% Formalin for 24 hours at 4 ^{0}C, embedded in paraffin and sectioned at 5 µm. Tissue sections were mounted on polylysine-coated microscopy slides. To assess the presence of collagen, serial sections were stained with picrosirius red according to standard histological procedures and analyzed using a light microscope (Zeiss or Nikon).

For immunofluorescence, sections were stained according to standard immunohistochemistry protocols (**Table 1**). Briefly, slides were deparaffinized in CitriSolv (Decon Labs, Inc), rehydrated and subjected to heat-induced epitope retrieval with Tris-EDTA (10mmol/L Tris + 1mmol/EDTA) or citrate (10mM citric acid, 0.02% Tween PH 6.0) buffer, respectively. Incubation with antibodies (**Table 1**) was followed by

visualization by incubation of different Alexa-conjugated fluorescent secondary antibodies (Invitrogen, see **Table 1**). Sections were mounted with Fluoromount-G mounting media with DAPI (glycoMATRIX).

Semi-quantitative analyses of the images were performed using ImageJ software and in-house designed Matlab scripts and a minimum of 8 images of random field per cardiac tissue were analyzed. The percentage fibrosis was determined with semi-quantification of picrosirius red staining and the percentage fibrosis was expressed as the average ratio of total collagen area divided by the total myocardial area of the whole image. The same approach was used to determine the percentage area staining positive for elastin. The numbers of cells expressing Fibronectin around the nucleus were counted using ImageJ. Comparison between pre- and post-LVAD groups for all patients were performed within the same staining procedure. To determine the percentage of cardiac fibroblasts in the myocardium, α-actinin and vimentin-positive cells were quantified by an in-house designed Matlab script counting number of "green" and "red" stained cells.

To determine the aspect ratio (AR) of the N-cadherin and Connexin 43 (Cx43) expression at the intercalated disc, an in-house Matlab script was designed. Images were semi-automated binarized to detect and measure the ellipses of intercalated discs using the Cx43 and N-cadherin markers. As a result of cardiac injury, redistribution of Cx43 to the intercalated discs on the lateral sides of the cardiomyocytes, results in a reduction of the aspect ratio of the ellipse, closer to a circular aspect ratio of 1.

All quantified data are presented as mean ± SD. Statistical analysis of the results was accomplished by the non-parametric Mann-Whitney test to compare the grouped samples. Statistical analysis was performed for multiple comparisons a Kruskall-Wallis assuming non-equal variances, with Dunn's post-hoc test. Statistical significance was considered when $P<0.05$. Graphics and statistical analysis were performed using the Graphpad Prism 5.04 software package (Graphpad Software). More information on the in-house designed Matlab script can be provided on request (m.c.v.turnhout@tue.nl).

Protein Extraction, Purification and Proteomics Analysis.

Mass spectrometry and data analysis methods have been described previously [69, 70]. In brief, for decellularized tissue, three non-failing and four failing human hearts were studied. Flash-frozen myocardium-derived decellularized scaffolds were pulverized in liquid nitrogen using a mortar and pestle. The pulverized tissue was then homogenized in lysis buffer (pH 7.5) containing 50 mmol/L Tris, 150 mmol/L NaCl, 0.3 % sodium dodecyl sulfate and 1 % protease inhibitors. Protein extraction was performed using TRIS-buffered saline with 0.3% sodium dodecyl sulfate followed by chloroform-methanol precipitation. Precipitated protein was dissolved in 0.1% RapiGest (Waters Corp) in 50 mM ammonium bicarbonate. Cysteines were reduced with dithiothreitol at 60 °C for 30 min, followed by bath sonication, and then boiled for 5 min to ensure proteins were dissolved. Cysteines were alkylated with iodoacetamide for 30 min at room temperature, with no centrifugations before digestion with porcine trypsin to minimize any loss of poorly soluble proteins. After RapiGest cleavage according to the manufacturer's directions, samples were centrifuged at 16,000 x G for 30 min to remove RapiGest Cleavage products. A digest with 50 fmol of yeast alcohol dehydrogenase was added as an internal detection control. Peptides were separated on NanoAcquity liquid chromatography coupled to a Synapt G2 HDMS quadrupole time-of-flight mass spectrometer (Waters Corp). Two 120 min liquid chromatography runs were performed with acetonitrile: water gradient for each biological replicate in resolution/ion mobility mode (traveling wave ion mobility spectrometry (TWIMS) (total of 14 LC/MS/MS chromatograms). Every 30s a lockmass spectrum of doubly charged Glu-1-Fibrinopeptide B at (m/z 785.8426) was recorded from the reference sprayer. Label-free quantitation was performed with Progenesis QI for Proteomics (Waters Corp.) with database search against a UniProt database of human sequences (release 2013_11) including porcine trypsin, yeast alcohol dehydrogenase and sheep keratin.

Raw mass spectrometry data are made available at the MassIVE repository (https://massive.ucsd.edu/) as dataset MSV000088676 with raw files located at ftp://massive.ucsd.edu/MSV000088676/.

Ischemic and non-ischemic tissues from cardiomyopathy patients were analyzed: NICM-PRE, NICM-POST, ICM-PRE, ICM-POST, Healthy (four biological replicates for all diseased samples, two replicates for healthy samples). Two LC/MS chromatograms were recorded for each biological replicate (a total of 36 LC/MS/MS chromatograms for 18 samples). Methods were the same as described above for decellularized tissues. Low amounts of protein in small CMCs grown in vitro necessitated mass spectrometry data collection in instrument sensitivity mode instead of resolution/ion mobility mode (TWIMS). Sensitivity data were analyzed with ProteinLynx Global Server V.2.5, RC9, (Waters Corp) followed by label-free intensity-based quantitation with Rosetta Elucidator software Ver. 3.3.0.1.SP3_CRE52.21 (Ceiba Solutions, Inc.) that employs the peptide teller algorithm as described previously [71].

Differential protein expressions and GSEA analysis of proteomic data for whole tissues were done using the iDEP web tool (version 0.92, http://bioinformatics.sdstate.edu/idep/#) [72]. Briefly, FDR and fold changes (FC) for proteins were analyzed with DESeq2. All differentially expressed proteins (FDR cutoff: limmaPval= 0.1; Fold-change cutoff: limmaFC= 1.3; Promoter analysis for DEGs: radio.promoter= 300 bp) were used to generate volcano plots and heatmaps. Volcano plots were generated with the web app, VolcaNoseR (https://huygens.science.uva.nl/VolcaNoseR/). Heatmaps were generated with a web server, Morpheus (https://software.broadinstitute.org/morpheus/). Pathway enrichment analysis was carried out through String API for Go Biological Process, Go Cellular Component, Go Molecular Function and KEGG at FDR cutoff=0.01. GSEA was carried out with the following parameters: FDR cutoff: pathwayPvalCutoff= 0.2; Min size for gene set: minSetSize= 15; Max size for gene set: maxSetSize= 2000.

RNA Seq

Total RNA was isolated using a Qiagen total RNA kit as per manufacturer protocol. After DNase treatment, RNA quality was assessed by bioanalyzer. RNA sequencing was performed with 40M depth at the Columbia Genome Center using the Illumina HiSeq 2500 platform. GSEA was carried out with GSEA tool from Broad Institute (http://www.gsea-msigdb.org/gsea/index.jsp).

Disclosure

The authors disclose no conflict of interest.

References:

1. Virani, S.S., et al., *Heart Disease and Stroke Statistics-2020 Update: A Report From the American Heart Association.* Circulation, 2020. **141**(9): p. e139-e596.
2. Follath, F., *Ischemic versus non-ischemic heart failure: should the etiology be determined?* Heart Fail Monit, 2001. **1**(4): p. 122-5.
3. Zhang, Z.H., et al., *Clinical characteristics and long-term prognosis of ischemic and non-ischemic cardiomyopathy.* Indian Heart J, 2020. **72**(2): p. 93-100.
4. Ng, A.C., et al., *Differences in management and outcome of ischemic and non-ischemic cardiomyopathy.* Int J Cardiol, 2008. **129**(2): p. 198-204.
5. Badylak, S.F., *The extracellular matrix as a scaffold for tissue reconstruction.* Seminars in Cell and Developmental Biology, 2002. **13**(5): p. 377-383.
6. Badylak, S.F., *Xenogeneic extracellular matrix as a scaffold for tissue reconstruction.* Transplant immunology, 2004. **12**(3-4): p. 367-377.

7. Davis, G.E., et al., *Regulation of tissue injury responses by the exposure of matricryptic sites within extracellular matrix molecules.* AJPA, 2000. **156**(5): p. 1489-1498.
8. Tønnessen, T. and C.W. Knudsen, *Surgical left ventricular remodeling in heart failure.* European Journal of Heart Failure, 2005. **7**(5): p. 704-709.
9. Lodish, H., et al., *Molecular Cell Biology 5th Edition, Modern Genetic Analysis 2nd Edition & Cd-rom*. 2004: W H Freeman & Company.
10. Fomovsky, G.M., S. Thomopoulos, and J.W. Holmes, *Contribution of extracellular matrix to the mechanical properties of the heart.* Journal of Molecular and Cellular Cardiology, 2009: p. 1-7.
11. Rienks, M., et al., *Myocardial extracellular matrix: an ever-changing and diverse entity.* Circ Res, 2014. **114**(5): p. 872-88.
12. van Putten, S., Y. Shafieyan, and B. Hinz, *Mechanical control of cardiac myofibroblasts.* J Mol Cell Cardiol, 2016. **93**: p. 133-42.
13. Huang, E., et al., *The Roles of Immune Cells in the Pathogenesis of Fibrosis.* International journal of molecular sciences, 2020. **21**(15): p. 5203.
14. Frangogiannis, N.G., *The Extracellular Matrix in Ischemic and Nonischemic Heart Failure.* Circ Res, 2019. **125**(1): p. 117-146.
15. Badylak, S.F., et al., *The use of extracellular matrix as an inductive scaffold for the partial replacement of functional myocardium.* Cell transplantation, 2006. **15 Suppl 1**: p. S29-40.
16. Ott, H.C., et al., *Perfusion-decellularized matrix: using nature's platform to engineer a bioartificial heart.* Nature medicine, 2008. **14**(2): p. 213-221.
17. Chang, Y., et al., *Tissue regeneration observed in a basic fibroblast growth factor-loaded porous acellular bovine pericardium populated with mesenchymal stem cells.* The Journal of Thoracic and Cardiovascular Surgery, 2007. **134**(1): p. 65-73. 73.e1-4.
18. Wei, H.-J., et al., *Porous acellular bovine pericardia seeded with mesenchymal stem cells as a patch to repair a myocardial defect in a syngeneic rat model.* Biomaterials, 2006. **27**(31): p. 5409-5419.
19. Badylak, S.F., *Regenerative medicine and developmental biology: the role of the extracellular matrix.* Anatomical record. Part B, New anatomist, 2005. **287**(1): p. 36-41.
20. Crapo, P.M. and Y. Wang, *Small intestinal submucosa gel as a potential scaffolding material for cardiac tissue engineering.* Acta Biomaterialia, 2010. **6**(6): p. 2091-2096.
21. Seif-Naraghi, S.B., et al., *Patient-to-patient variability in autologous pericardial matrix scaffolds for cardiac repair.* Journal of cardiovascular translational research, 2011. **4**(5): p. 545-556.
22. Freytes, D.O., et al., *Preparation and rheological characterization of a gel form of the porcine urinary bladder matrix.* Biomaterials, 2008. **29**(11): p. 1630-1637.
23. Lin, Y.D., et al., *Instructive Nanofiber Scaffolds with VEGF Create a Microenvironment for Arteriogenesis and Cardiac Repair.* Science Translational Medicine, 2012. **4**(146): p. 146ra109-146ra109.
24. Duan, Y., et al., *Hybrid Gel Composed of Native Heart Matrix and Collagen Induces Cardiac Differentiation of Human Embryonic Stem Cells without Supplemental Growth Factors.* Journal of cardiovascular translational research, 2011. **4**(5): p. 605-615.
25. Freytes, D.O., et al., *Natural cardiac extracellular matrix hydrogels for cultivation of human stem cell-derived cardiomyocytes.* Methods Mol Biol, 2014. **1181**: p. 69-81.
26. Godier-Furnemont, A.F., et al., *Composite scaffold provides a cell delivery platform for cardiovascular repair.* Proc Natl Acad Sci U S A, 2011. **108**(19): p. 7974-9.
27. Critsinelis, A., et al., *Left Ventricular Recovery with Explantation of Continuous-Flow Left Ventricular Assist Device after 5 Years of Support.* Ann Thorac Cardiovasc Surg, 2021. **27**(3): p. 211-214.
28. Goldstein, D.J., et al., *Young patients with nonischemic cardiomyopathy have higher likelihood of left ventricular recovery during left ventricular assist device support.* J Card Fail, 2012. **18**(5): p. 392-5.

29. Wever-Pinzon, O., et al., *Cardiac Recovery During Long-Term Left Ventricular Assist Device Support.* J Am Coll Cardiol, 2016. **68**(14): p. 1540-53.
30. Birks, E.J., et al., *Prospective Multicenter Study of Myocardial Recovery Using Left Ventricular Assist Devices (RESTAGE-HF [Remission from Stage D Heart Failure]): Medium-Term and Primary End Point Results.* Circulation, 2020. **142**(21): p. 2016-2028.
31. Frazier, O.H., et al., *Ventricular reconditioning and pump explantation in patients supported by continuous-flow left ventricular assist devices.* J Heart Lung Transplant, 2015. **34**(6): p. 766-72.
32. Engler, A.J., et al., *Matrix elasticity directs stem cell lineage specification.* Cell, 2006. **126**(4): p. 677-89.
33. Zhang, W., Y. Liu, and H. Zhang, *Extracellular matrix: an important regulator of cell functions and skeletal muscle development.* Cell Biosci, 2021. **11**(1): p. 65.
34. Kosuge, M., et al., *Serum amyloid A is a better predictor of clinical outcomes than C-reactive protein in non-ST-segment elevation acute coronary syndromes.* Circ J, 2007. **71**(2): p. 186-90.
35. Johnson, B.D., et al., *Serum amyloid A as a predictor of coronary artery disease and cardiovascular outcome in women: the National Heart, Lung, and Blood Institute-Sponsored Women's Ischemia Syndrome Evaluation (WISE).* Circulation, 2005. **109**(6): p. 726-32.
36. Lepper, P.M., et al., *Lipopolysaccharide-binding protein (LBP) is associated with total and cardiovascular mortality in individuals with or without stable coronary artery disease--results from the Ludwigshafen Risk and Cardiovascular Health Study (LURIC).* Atherosclerosis, 2011. **219**(1): p. 291-7.
37. Murray, J., et al., *The subunit composition of the human NADH dehydrogenase obtained by rapid one-step immunopurification.* J Biol Chem, 2003. **278**(16): p. 13619-22.
38. Loeffen, J.L., et al., *cDNA of eight nuclear encoded subunits of NADH:ubiquinone oxidoreductase: human complex I cDNA characterization completed.* Biochem Biophys Res Commun, 1998. **253**(2): p. 415-22.
39. Bai, F., L. Wang, and M. Kawai, *A study of tropomyosin's role in cardiac function and disease using thin-filament reconstituted myocardium.* J Muscle Res Cell Motil, 2013. **34**(3-4): p. 295-310.
40. Yang, W., et al., *Reynoutrin Improves Ischemic Heart Failure in Rats Via Targeting S100A1.* Front Pharmacol, 2021. **12**: p. 703962.
41. Ritterhoff, J. and P. Most, *Targeting S100A1 in heart failure.* Gene Ther, 2012. **19**(6): p. 613-21.
42. Alvarez, B.V., et al., *Quantification of carbonic anhydrase gene expression in ventricle of hypertrophic and failing human heart.* BMC Cardiovasc Disord, 2013. **13**: p. 2.
43. Torella, D., et al., *Carbonic anhydrase activation is associated with worsened pathological remodeling in human ischemic diabetic cardiomyopathy.* J Am Heart Assoc, 2014. **3**(2): p. e000434.
44. Thompson, S.A., et al., *Acute slowing of cardiac conduction in response to myofibroblast coupling to cardiomyocytes through N-cadherin.* J Mol Cell Cardiol, 2014. **68**: p. 29-37.
45. Zhang, K., et al., *Asporin is a Potential Promising Biomarker for Common Heart Failure.* DNA Cell Biol, 2021. **40**(2): p. 303-315.
46. Zhao, Y., et al., *A Platform for Generation of Chamber-Specific Cardiac Tissues and Disease Modeling.* Cell, 2019. **176**(4): p. 913-927 e18.
47. Ronaldson-Bouchard, K., et al., *Advanced maturation of human cardiac tissue grown from pluripotent stem cells.* Nature, 2018. **556**(7700): p. 239-243.
48. Richards, D.J., et al., *Human cardiac organoids for the modelling of myocardial infarction and drug cardiotoxicity.* Nat Biomed Eng, 2020. **4**(4): p. 446-462.
49. Bader, B.L., et al., *Compound genetic ablation of nidogen 1 and 2 causes basement membrane defects and perinatal lethality in mice.* Mol Cell Biol, 2005. **25**(15): p. 6846-56.
50. Kim, E.H., et al., *Differential protein expression and basal lamina remodeling in human heart failure.* Proteomics Clin Appl, 2016. **10**(5): p. 585-96.

51. Batlle, M., et al., *Decreased expression of thrombospondin-1 in failing hearts may favor ventricular remodeling.* Transplant Proc, 2009. **41**(6): p. 2231-3.
52. Takemoto, S., et al., *Increased expression of dermatopontin mRNA in the infarct zone of experimentally induced myocardial infarction in rats: comparison with decorin and type I collagen mRNAs.* Basic Res Cardiol, 2002. **97**(6): p. 461-8.
53. Ahmed, A., et al., *Prolargin and matrix metalloproteinase-2 in heart failure after heart transplantation and their association with haemodynamics.* ESC Heart Fail, 2020. **7**(1): p. 223-234.
54. van Dijk, A., et al., *Accumulation of fibronectin in the heart after myocardial infarction: a putative stimulator of adhesion and proliferation of adipose-derived stem cells.* Cell Tissue Res, 2008. **332**(2): p. 289-98.
55. Valiente-Alandi, I., et al., *Inhibiting Fibronectin Attenuates Fibrosis and Improves Cardiac Function in a Model of Heart Failure.* Circulation, 2018. **138**(12): p. 1236-1252.
56. Protti, A., et al., *Assessment of Myocardial Remodeling Using an Elastin/Tropoelastin Specific Agent with High Field Magnetic Resonance Imaging (MRI).* J Am Heart Assoc, 2015. **4**(8): p. e001851.
57. Nehra, S., R.J. Gumina, and S.S. Bansal, *Immune cell Dilemma in Ischemic Cardiomyopathy: To Heal or Not to Heal.* Curr Opin Physiol, 2021. **19**: p. 39-46.
58. Tschumperlin, D.J., et al., *Mechanosensing and fibrosis.* J Clin Invest, 2018. **128**(1): p. 74-84.
59. Chopra, A., et al., *Cardiac myocyte remodeling mediated by N-cadherin-dependent mechanosensing.* Am J Physiol Heart Circ Physiol, 2011. **300**(4): p. H1252-66.
60. Quinn, T.A. and P. Kohl, *Cardiac Mechano-Electric Coupling: Acute Effects of Mechanical Stimulation on Heart Rate and Rhythm.* Physiol Rev, 2021. **101**(1): p. 37-92.
61. Quinn, T.A., *Cardiac mechano-electric coupling: a role in regulating normal function of the heart?* Cardiovasc Res, 2015. **108**(1): p. 1-3.
62. Lock, R., et al., *A framework for developing sex-specific engineered heart models.* Nat Rev Mater, 2021: p. 1-19.
63. Wan, L.Q., et al., *Micropatterned mammalian cells exhibit phenotype-specific left-right asymmetry.* Proc Natl Acad Sci U S A, 2011. **108**(30): p. 12295-300.
64. Yang, L., et al., *Human cardiovascular progenitor cells develop from a KDR+ embryonic-stem-cell-derived population.* Nature, 2008. **453**(7194): p. 524-8.
65. Yang, L., et al., *Human cardiovascular progenitor cells develop from a KDR+ embryonic-stem-cell-derived population.* Nature, 2008. **453**(7194): p. 524-528.
66. Yazawa, M., et al., *Using induced pluripotent stem cells to investigate cardiac phenotypes in Timothy syndrome.* Nature, 2011. **471**(7337): p. 230-4.
67. Eng, G., et al., *Autonomous beating rate adaptation in human stem cell-derived cardiomyocytes.* Nat Commun, 2016. **7**: p. 10312.
68. Kamgoue, A., et al., *Quantification of cardiomyocyte contraction based on image correlation analysis.* Cytometry A, 2009. **75**(4): p. 298-308.
69. Moran, D., et al., *Data-independent acquisition (MSE) with ion mobility provides a systematic method for analysis of a bacteriophage structural proteome.* J Virol Methods, 2014. **195**: p. 9-17.
70. Lin, M.K., et al., *HTRA1, an age-related macular degeneration protease, processes extracellular matrix proteins EFEMP1 and TSP1.* Aging Cell, 2018. **17**(4): p. e12710.
71. Alegre-Aguaron, E., et al., *Growth factor priming differentially modulates components of the extracellular matrix proteome in chondrocytes and synovium-derived stem cells.* PLoS One, 2014. **9**(2): p. e88053.
72. Ge, S.X., E.W. Son, and R. Yao, *iDEP: an integrated web application for differential expression and pathway analysis of RNA-Seq data.* BMC Bioinformatics, 2018. **19**(1): p. 534.

Acknowledgements

The authors would like to thank Dr. Mark C. van Turnhout for the in-house designed Matlab scripts. David Chen for initial processing of the mass spectrometry data and Davey Liu for uploading the raw mass spectrometry files to the data archive. This paper is dedicated to memory of Andrey Bondarenko (01/06/1968 - 5/27/2019), the developer and architect of the Rosetta Elucidator software who helped our team learn and perform proteomic data analysis.

Funding sources

This work was supported by the Schwartz Foundation [to AGF, BF and GVN], National Institutes of Health [R01 HL076485 to GVN, UH3 EB025765 to GVN, P41 EB027062 to GVN, K08HL140201 to BF]; National Science Foundation [NSF16478 to GVN]; European Molecular Biology Organization [EMBO ASTF 497-2012 to Nbax], the Dutch Heart Foundation [DHF-2014T013 to Nbax], and Natural Sciences and Engineering Research Council of Canada Postdoctoral fellowship [to YZhao]; We thank the New York State Stem Cell Science Board (NYSTEM) for support under contract #C02361 (GVN and LMB) with matching funds from Columbia University for funding of the mass spectrometer.

Tables

Table 1. Details on immunostaining

Antigen	Source	Isotype	Species	Antigen Retrieval	Blocking agent	Dilution solution	Dilution	Label
α-Actinin	SA (A7811)	IgG1	Mouse	Tris-EDTA (pH9.0)	10% Horse serum	1% Horse serum	1:500	-
Vimentin	CS (clone D21H3, #5741)	IgG	Rabbit	Tris-EDTA (pH9.0)	10% Horse serum	1% Horse serum	1:100	-
Connexin 43 (Cx43)	SA (C6219)	IgG	Rabbit	Antigen Unmasking Solution	5% BSA	1% BSA	1:200	-
C19	provided by Leung al.	IgM	Mouse	Antigen Unmasking Solution	5% BSA	1% BSA	1:250	
N-cadherin	MP (clone EPR1792y, 04-1126)	IgG	Rabbit	Citrate Buffer (pH6.0)	10% Horse serum	1% Horse serum	1:200	-
				Antigen Unmasking Solution	5% BSA	1% BSA	1:200	
cTroponinI		IgG	Rabbit	Antigen Unmasking Solution	5% BSA	1% BSA	1:250	
Vinculin	SA (V9131A7811)	IgG1	Mouse	Citrate Buffer (pH6.0)	10% Horse serum	1% Horse serum	1:500	-
Elastin	Abcam (ab21610)	IgG	Rabbit	Citrate Buffer (pH6.0)	10% Horse serum	1% Horse serum	1:200	-
Fibronectin	SA (F3648)	IgG	Rabbit	Tris-EDTA (pH9.0)	10% Horse serum	1% Horse serum	1:200	-
Mouse IgG1	IG (A21123)	IgG1	Goat	-	-	1% Horse serum or PBS	1:300	Alexa Fluor 546
Mouse IgM	Abcam (ab150121)	IgM	Donkey	-	-	1% BSA	1:250	Alexa Fluor 488
Rabbit IgG	IG (A37118)	IgG	Donkey	-	-	1% Horse serum or PBS	1:300	Alexa Fluor 488
Rabbit IgG	IG (A31572)	IgG	Donkey	-	-	PBS	1:300	Alexa Fluor 555
Rabbit IgG	IG (A31573)	IgG	Donkey	-	-	1% BSA	1:200	Alexa Fluor 647

Supplemental Table 1: Peptide counts and protein identification summary for decellularized scaffolds.

Supplemental Table 2: Peptide counts and protein identification summary for whole heart tissues.

Supplemental Table 3: RNAseq dataset for whole heart tissues.

Figure captions

Figure 1: Experimental Design Overview. Healthy and heart failure patient samples were decellularized, sectioned and seeded with stem cell derived cardiomyocytes (CM). A disease-like phenotypic and functional modulation through the ECM from heart failure patient samples was demonstrated with previously healthy CMs. In addition, heart failure patient samples were profiled and compared at a molecular level to understand the etiological differences between NICM and ICM and the therapeutic potential of LVAD.

Figure 2: Proteomics reveals differences in ECM composition and protein expression between Non-Failing and Failing human hearts. A) overview; B) heart explant and the processed decellularized ECM; C) Principal component analysis of proteomics obtained from decellularized ECMs of non-failing and failing patient samples; D) Volcano plots indicating significantly altered proteins identified in the proteomic datasets from decellularized ECMs of non-failing and failing hearts. Negative log-transformed P-values (two-tailed Student's t-test associated with individual proteins plotted against the difference in means of log2-transformed normalized values for individual proteins. E) Heat map representing the expression of selected ECM proteins across non-failing and failing patient samples. F) Representative histology staining for ECM proteins from non-failing and failing patient samples, including vitronectin, nidogen, laminin and Picro Sirius Red for collagen. Patient samples involved were HH1, HH2 and HH3 (n=3) for non-failing ECMs and 13B, 22B, 24B,and 28B, (n=4) for failing ECMs (ICM after LVAD)

Figure 3: ECM from non-failing and failing hearts has different al effects on morphology and function of cultured cardiomyocytes. A) illustration of using decellularized ECM as a scaffold to create engineered cardiac tissue. B) Representative bright-field image of engineered heart tissue using ECM-derived scaffold. C) Cumulative strain was evaluated on CMC with different doses of isoproterenol, Mann Whitney test, p=0.13. D) Confocal images of CMC grown using ECM from non-failing and failing heart patients stained with a-actinin (green), fibronectin (red), and Troponin (red), scale bar=100 mm E) Heatmap of differential expressed proteins between non-failing and failing heart patient samples, including proteins that constitute cardiac-specific contractile filaments and cytoskeletal components, as well as the ones responsible of mitochondria energy production. Patient samples involved were HH1 and HH2 (n=2) for non-failing samples and 13B, 22B, 24B, and 28B, (n=4) for failing samples (ICM after LVAD)

Figure 4: Differences in proteomics and RNASeq between tissues from ischemic and non-ischemic heart failure patients A) Heart failure can have different etiologies, such as ICM and NICM. B) Principal component analysis of whole tissue proteomics of non-failing and failing heart patient samples showed clear segregation of two types of heart failure conditions. C) Venn diagram reveals the overlap of significantly enriched annotations among datasets (FDR < 0.1, minimum fold change=1.3). D) Volcano plots indicating significantly altered proteins identified in the proteomic datasets from whole tissue proteomics. Negative log-transformed P-values (two-tailed Student's t-test) associated with individual proteins plotted against the difference in means of log2-transformed normalized values for individual proteins. E) Differentially expressed genes in GO terms and KEGG were identified via the STRING API [56] for enrichment analysis, where enrichment in ICMpre (ICM before LVAD surgery) is demonstrated in red bars and NICMpre (NICM before LVAD) is blue bars. F) Heatmap representing the differential expressed proteins across ICM and NICM patient samples. G) GSEA pathway analysis of proteomics (biological process) demonstrates the enriched pathways in ICMpre (green) and NICMpre (red) using pathway tree. Patient samples were 8A, 34A, 7A, and 27A (n=4) for NICM whole heart tissues and 9A, 23A, 31A, and 65A, (n=4) from ICM whole heart tissues, both before LVAD.

Figure 5: LVAD procedure attenuates NICM disease phenotype, as demonstrated by proteomics and RNASeq data analysis. A) Patient samples were collected during LVAD surgery (NICMpre, heart tissues before LVAD support) and after transplantation (NICMpo, heart tissues after a significant period of LVAD support). B) Principal component analysis of whole tissue proteomics of NICMpre and NICMpo, suggesting potential segregation between NICMpre and NICMpo. C) Venn diagram reveals the overlap of significantly enriched annotations among datasets (FDR < 0.1, minimum fold change=1.3). NICMpo-H had 60% fewer differential expressed proteins compared to NICMpre-H. D) Volcano plots indicating significantly altered proteins identified by whole tissue proteomic analysis of NICMpre and NICMpo tissues. Negative log-transformed P-values (two-tailed Student's t-test) associated with individual proteins plotted against the difference in means of log2-transformed normalized values for individual proteins. E) Heatmap representing the differential expressed proteins in tissues from NICMpre and NICMpo patients. F) Differentially expressed genes in GO terms were identified via the STRING API [56] for enrichment analysis; enrichment in NICMpre and NICMpo are demonstrated by blue bars and red bars, respectfully. G) GSEA pathway analysis of proteomics using a pathway tree demonstrates enriched pathways in NICMpre (green) and NICMpo (red) tissues. Patient samples were 8A, 34A, 7A, and 27A (n=4) for NICM before LVAD and 7B, 27B, 33B, and 50B, (n=4) from ICM after LVAD

Figure 6: LVAD procedures do not influence disease phenotypes in ICM patients. A) Patient samples were collected during LVAD surgery (ICMpre, heart tissues before LVAD support) and after transplantation (ICMpo, heart tissues after a significant period of LVAD support). B) Principal component analysis of whole tissue proteomics of ICMpre and ICMpo, suggested no segregation between ICMpre and ICMpo. C) Volcano plots indicating significantly altered proteins identified from whole tissue proteomics between ICMpre and ICMpo. Negative log-transformed P-values (two-tailed Student's t-test) associated with individual proteins plotted against the difference in means of log2-transformed normalized values for individual proteins. Venn diagram reveals the overlap of significantly enriched (FDR < 0.1, minimum fold change=1.3) annotations among datasets, where ICMpo-H has slightly fewer differential expressed proteins than ICMpre-H. D) Differentially expressed genes in GO terms were identified via the STRING API [56] for enrichment analysis. E) Heatmap representing the differentially expressed proteins in ICMpre and ICMpo patient samples. F) GSEA pathway analysis of proteomics demonstrates the enriched pathways in ICMpo (green) and ICMpre (red) using a pathway tree. Patient samples were 9A, 23A, 31A, and 6A (n=4) for ICM whole heart tissues harvested before LVAD and 13B, 22B, 24B, and 28B, (n=4) from ICM whole heart tissues harvested after LVAD.

Supplemental Figure captions

Supplemental Figure 1: Sample summary

Supplemental Figure 2: Comparison using RNAseq dataset between ICM and NICM patient tissues. A) PCA shows a clear separation between groups. B) Correlation-distance-based hierarchical clustering of 1,000 most variable genes between ICM and NICM. C) GSEA demonstrated that genes related to cardiac action potential and contractile function are enriched in ICM samples. There are also genes related to cardiac fibroblasts, ventricular arrhythmia and fetal cardiomyocytes in ICM samples, suggesting potential fibroblast proliferation and cardiomyocyte reversal to fetal-like state due to injury. Patient samples were 6A and 60A (n=2) for NICM whole heart tissues and 41A and 82A (n=2) from ICM whole heart tissues, both before LVAD.

Supplemental Figure 3: Representative IHC images of NICM and ICM samples, before and after LVAD procedures. A) Troponin T (green) and N-cadherin (red) staining combined with the quantification of B) N-cadherin alignment in matching patient samples before and after LVAD procedure. The presence of both Troponin T and N-cadherin increased NICM samples during LVAD support, while it deteriorated in ICM samples. Paired t-test was performed between NICMpre and NICMpo only. C) Picro Sirius red staining for visualization and D) quantifications of collagen in the matched patient samples. Both NICM and ICM showed trends of decreased collagen deposition during LVAD support. E, F) The ECM protein Fibronectin (in red) showed a trend of increase in expression around the nucleus in both ICM and NICM samples after LVAD support. Nuclei are stained with DAPI (blue). Scale bar: 50 µm (A and E) and 100 µm (C). Patient samples were 6, 7, 27, and 29 (n=4) for NICM and 31, 41, 53, and 82, (n=4) for ICM. All four matched samples in each group are compared before and after LVAD.

Supplemental Figure 4: Comparison of NICMpre and NICMpo patient tissues using RNAseq dataset. A) PCA plots indicating the separation of NICMpre and NICMpo relative to non-failing samples, respectively. B) Correlation distance-based hierarchical clustering of 1,000 most variable genes between NICMpre, NICMpo, and H (non-failing), in which NICMpost samples cluster closer to H compared to NICMpre. C) GSEA reveals significantly enriched gene sets related to cardiac contraction and the contractile machinery in NICMpo samples when compared with NICMpre. Negative enrichment of a-, g-interferon and mitochondria-related gene sets were also observed in NICMpo samples. Patient samples were non-failing heart tissues, HH1 and HH2 (n=2), and matched NICM samples of 6 and 60 from before and after LVAD (n=2).

Supplemental Figure 5: Comparison of ICMpre and ICMpo patient tissues using RNAseq dataset. A) PCA plots indicating the separation of ICMpre and ICMpo relative to non-failing samples, respectively. B) Correlation-distance-based hierarchical clustering of 1000 most variable genes between ICMpre, ICMpo and H (non-failing). C) GSEA also reveals significantly enriched gene sets related to ECM membrane receptors, ECM remodeling and collagen synthesis in ICMpo samples. Patient samples were non-failing heart tissues, HH1 and HH2 (n=2), matched ICM samples of 41 and 82 from before and after LVAD (n=2).

Antigen	Source	Isotype	Species	Antigen Retrieval	Blocking agent	Dilution solution	Dilution	Label
α-Actinin	SA (A7811)	IgG1	Mouse	Tris-EDTA (pH9.0)	10% Horse serum	1% Horse serum	1:500	-
Vimentin	CS (clone D21H3, #5741)	IgG	Rabbit	Tris-EDTA (pH9.0)	10% Horse serum	1% Horse serum	1:100	-
Connexin 43 (Cx43)	SA (C6219)	IgG	Rabbit	Antigen Unmasking Solution	5% BSA	1% BSA	1:200	-
C19	provided by Leung *al.*	IgM	Mouse	Antigen Unmasking Solution	5% BSA	1% BSA	1:250	
N-cadherin	MP (clone EPR1792y, 04-1126)	IgG	Rabbit	Citrate Buffer (pH6.0)	10% Horse serum	1% Horse serum	1:200	-
Vinculin	SA (V9131A7811)	IgG1	Mouse	Citrate Buffer (pH6.0)	10% Horse serum	1% Horse serum	1:500	-
Elastin	Abcam (ab21610)	IgG	Rabbit	Citrate Buffer (pH6.0)	10% Horse serum	1% Horse serum	1:200	-
Fibronectin	SA (F3648)	IgG	Rabbit	Tris-EDTA (pH9.0)	10% Horse serum	1% Horse serum	1:200	-
Mouse IgG1	IG (A21123)	IgG1	Goat	-	-	1% Horse serum or PBS	1:300	Alexa Fluor 546
Mouse IgM	Abcam (ab150121)	IgM	Donkey		-	1% BSA	1:250	Alexa Fluor 488
Rabbit IgG	IG (A37118)	IgG	Donkey	-	-	1% Horse serum or PBS	1:300	Alexa Fluor 488
Rabbit IgG	IG (A31572)	IgG	Donkey	-	-	PBS	1:300	Alexa Fluor 555
Rabbit IgG	IG (A31573)	IgG	Donkey	-	-	1% BSA	1:200	Alexa Fluor 647

Highlights

- Non-ischemic and ischemic myocardium display differences in the composition of extracellular matrix and respond differently to mechanical unloading by a left ventricular assist device (LVAD)
- The changes in extracellular matrix in failing hearts affect the morphology and function of human stem cell derived cardiomyocytes
- Ventricular unloading of non-ischemic hearts induces upregulation of proteins related to cardiac function
- Ventricular unloading of ischemic hearts induces upregulation of ECM proteins without reverse remodeling

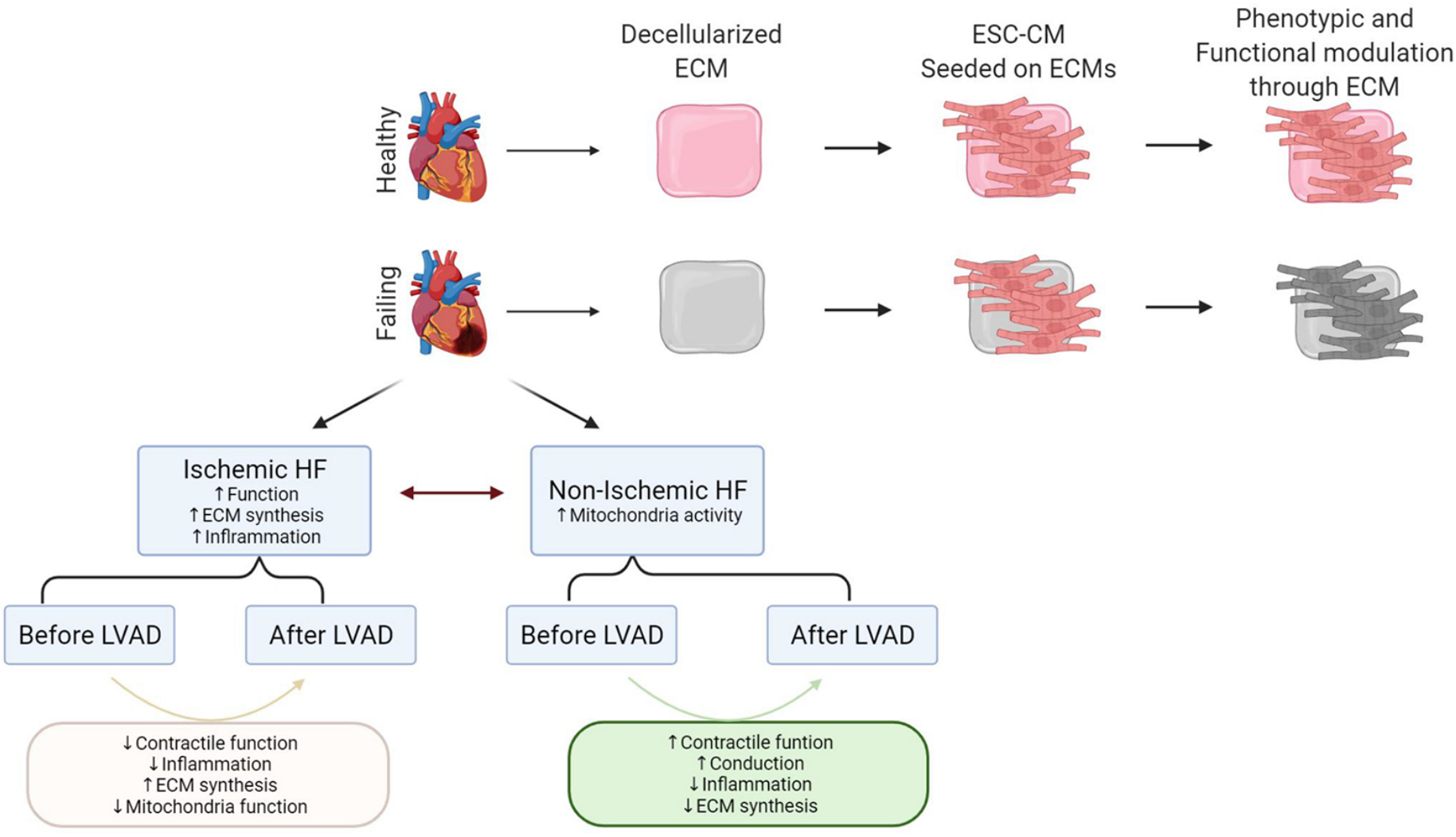

Graphics Abstract

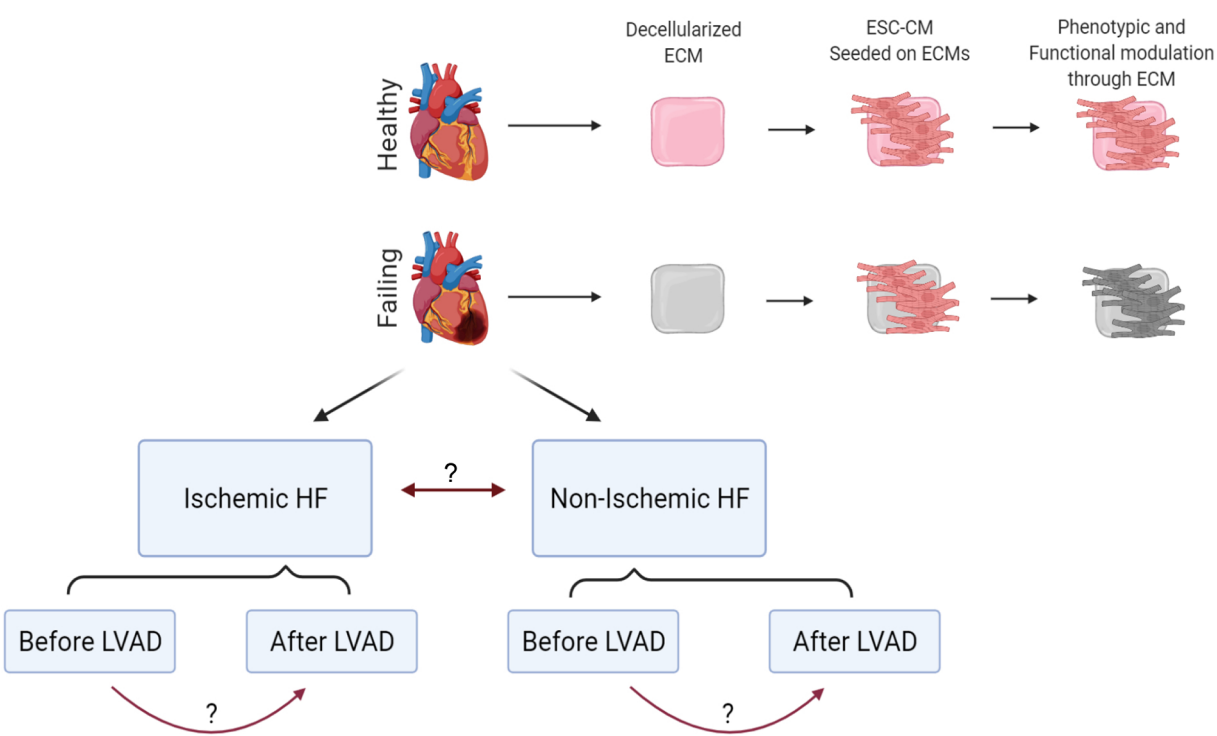
Decellularized ECM
ESC-CM Seeded on ECMs
Phenotypic and Functional modulation through ECM
Healthy
Failing
Ischemic HF
?
Non-Ischemic HF
Before LVAD
After LVAD
?
Before LVAD
After LVAD
?

Figure 1

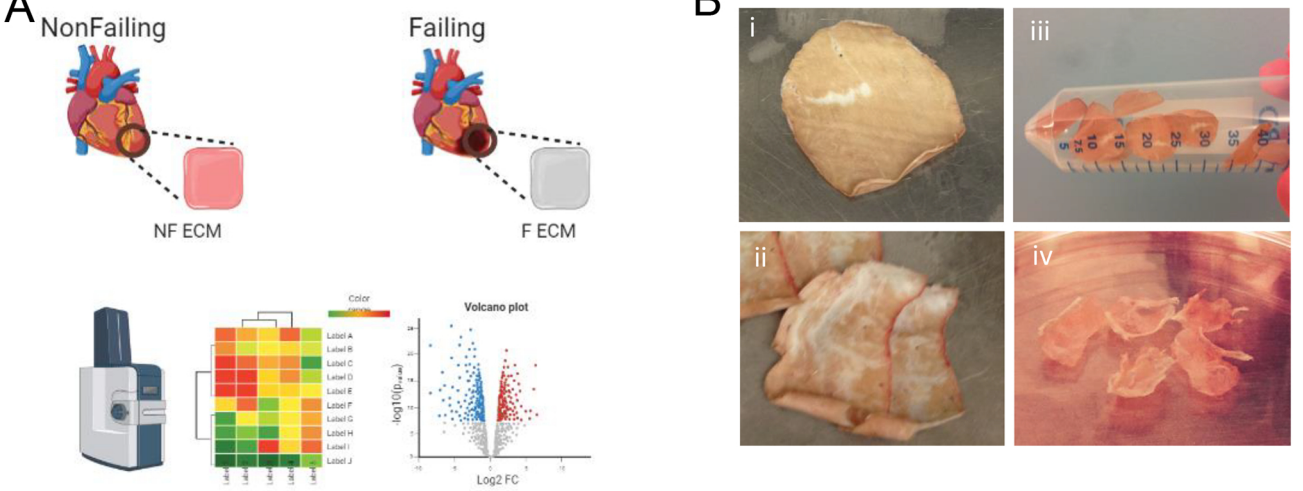
A
NonFailing
Failing
NF ECM
F ECM
Volcano plot
Log2 FC
B
i
iii
ii
iv

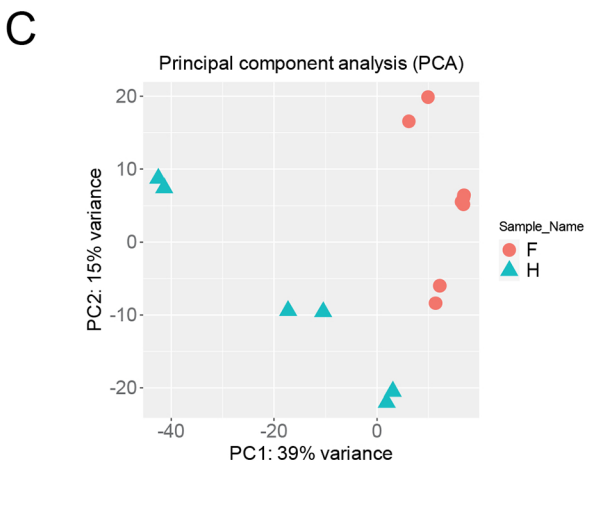
C
Principal component analysis (PCA)
PC2: 15% variance
PC1: 39% variance
Sample_Name
F
H

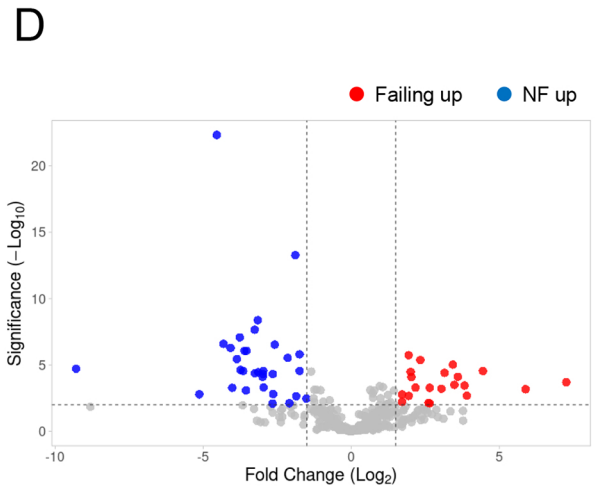
D
Failing up
NF up
Significance (−Log10)
Fold Change (Log2)

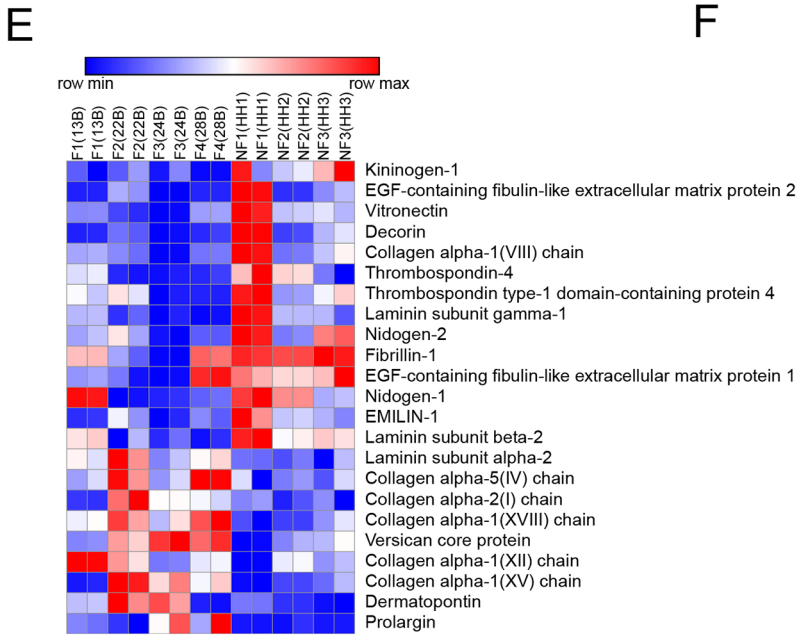
E
row min
row max
F1(13B)
F1(13B)
F2(22B)
F2(22B)
F3(24B)
F3(24B)
F4(28B)
F4(28B)
NF1(HH1)
NF1(HH1)
NF2(HH2)
NF2(HH2)
NF3(HH3)
NF3(HH3)
Kininogen-1
EGF-containing fibulin-like extracellular matrix protein 2
Vitronectin
Decorin
Collagen alpha-1(VIII) chain
Thrombospondin-4
Thrombospondin type-1 domain-containing protein 4
Laminin subunit gamma-1
Nidogen-2
Fibrillin-1
EGF-containing fibulin-like extracellular matrix protein 1
Nidogen-1
EMILIN-1
Laminin subunit beta-2
Laminin subunit alpha-2
Collagen alpha-5(IV) chain
Collagen alpha-2(I) chain
Collagen alpha-1(XVIII) chain
Versican core protein
Collagen alpha-1(XII) chain
Collagen alpha-1(XV) chain
Dermatopontin
Prolargin

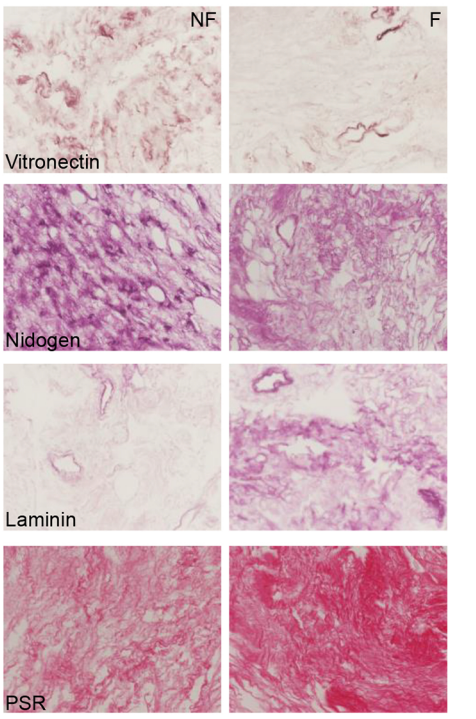
F
NF
F
Vitronectin
Nidogen
Laminin
PSR

Figure 2

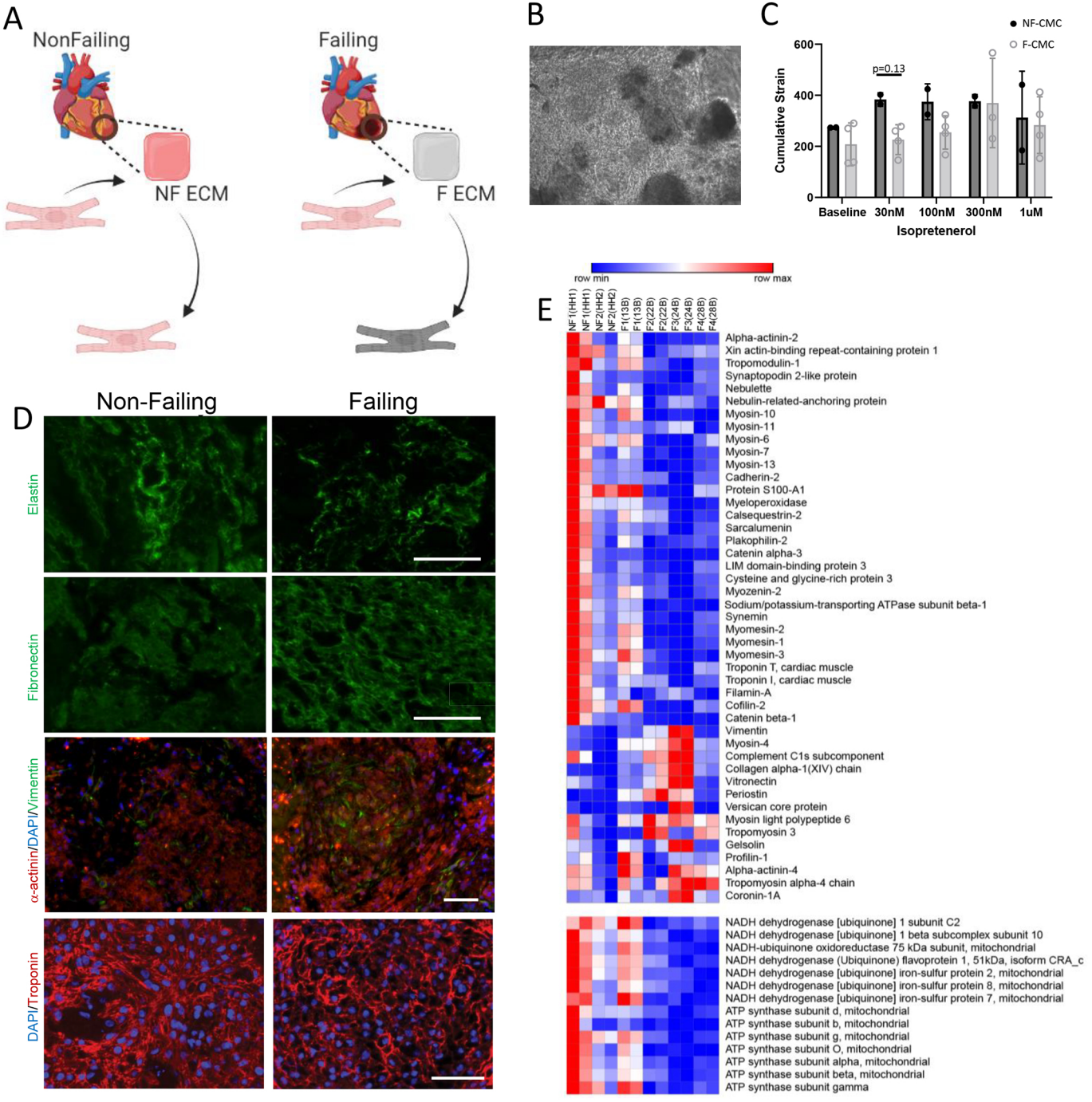
A
NonFailing
Failing
NF ECM
F ECM
B
C
NF-CMC
F-CMC
Cumulative Strain
600
400
200
0
p=0.13
Baseline
30nM
100nM
300nM
1uM
Isopretenerol
D
Non-Failing
Failing
Elastin
Fibronectin
α-actinin/DAPI/Vimentin
DAPI/Troponin
E
row min
row max
NF1(HH1)
NF1(HH1)
NF2(HH2)
NF2(HH2)
F1(13B)
F1(13B)
F2(22B)
F2(22B)
F3(24B)
F3(24B)
F4(28B)
F4(28B)
Alpha-actinin-2
Xin actin-binding repeat-containing protein 1
Tropomodulin-1
Synaptopodin 2-like protein
Nebulette
Nebulin-related-anchoring protein
Myosin-10
Myosin-11
Myosin-6
Myosin-7
Myosin-13
Cadherin-2
Protein S100-A1
Myeloperoxidase
Calsequestrin-2
Sarcalumenin
Plakophilin-2
Catenin alpha-3
LIM domain-binding protein 3
Cysteine and glycine-rich protein 3
Myozenin-2
Sodium/potassium-transporting ATPase subunit beta-1
Synemin
Myomesin-2
Myomesin-1
Myomesin-3
Troponin T, cardiac muscle
Troponin I, cardiac muscle
Filamin-A
Cofilin-2
Catenin beta-1
Vimentin
Myosin-4
Complement C1s subcomponent
Collagen alpha-1(XIV) chain
Vitronectin
Periostin
Versican core protein
Myosin light polypeptide 6
Tropomyosin 3
Gelsolin
Profilin-1
Alpha-actinin-4
Tropomyosin alpha-4 chain
Coronin-1A
NADH dehydrogenase [ubiquinone] 1 subunit C2
NADH dehydrogenase [ubiquinone] 1 beta subcomplex subunit 10
NADH-ubiquinone oxidoreductase 75 kDa subunit, mitochondrial
NADH dehydrogenase (Ubiquinone) flavoprotein 1, 51kDa, isoform CRA_c
NADH dehydrogenase [ubiquinone] iron-sulfur protein 2, mitochondrial
NADH dehydrogenase [ubiquinone] iron-sulfur protein 8, mitochondrial
NADH dehydrogenase [ubiquinone] iron-sulfur protein 7, mitochondrial
ATP synthase subunit d, mitochondrial
ATP synthase subunit b, mitochondrial
ATP synthase subunit g, mitochondrial
ATP synthase subunit O, mitochondrial
ATP synthase subunit alpha, mitochondrial
ATP synthase subunit beta, mitochondrial
ATP synthase subunit gamma

Figure 3

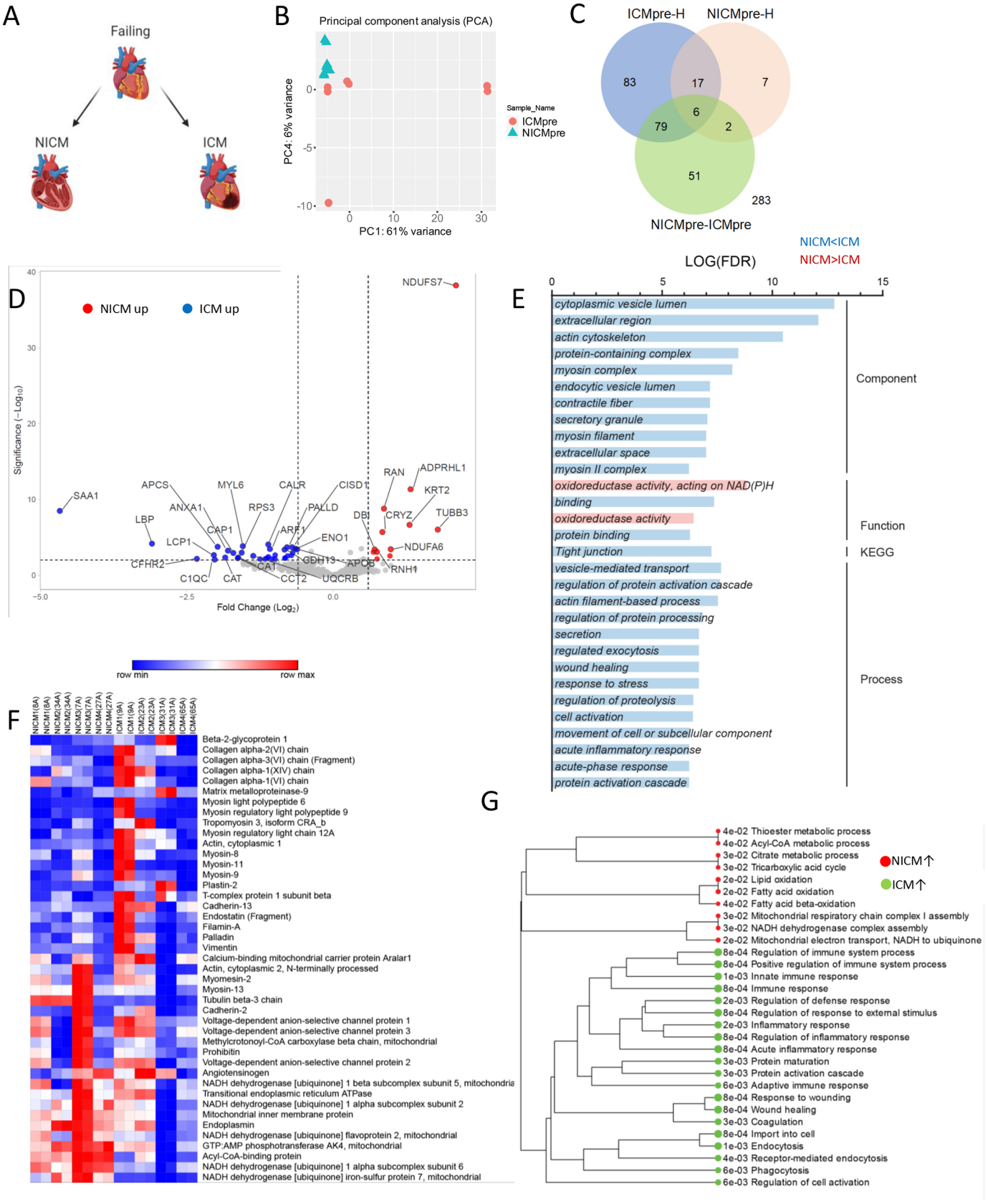
A
Failing
NICM
ICM
B
Principal component analysis (PCA)
PC4: 6% variance
PC1: 61% variance
Sample_Name
ICMpre
NICMpre
C
ICMpre-H
NICMpre-H
83
17
7
6
79
2
51
283
NICMpre-ICMpre
D
NICM up
ICM up
Significance (−Log10)
Fold Change (Log2)
NDUFS7
SAA1
APCS
MYL6
CALR
CISD1
RAN
ADPRHL1
KRT2
ANXA1
RPS3
PALLD
DBI
CRYZ
TUBB3
LBP
CAP1
ARF1
ENO1
LCP1
NDUFA6
CFHR2
GDI1
APOB
CAT
RNH1
C1QC
CAT
CCT2
UQCRB
E
LOG(FDR)
NICM<ICM
NICM>ICM
cytoplasmic vesicle lumen
extracellular region
actin cytoskeleton
protein-containing complex
myosin complex
endocytic vesicle lumen
contractile fiber
secretory granule
myosin filament
extracellular space
myosin II complex
oxidoreductase activity, acting on NAD(P)H
binding
oxidoreductase activity
protein binding
Tight junction
vesicle-mediated transport
regulation of protein activation cascade
actin filament-based process
regulation of protein processing
secretion
regulated exocytosis
wound healing
response to stress
regulation of proteolysis
cell activation
movement of cell or subcellular component
acute inflammatory response
acute-phase response
protein activation cascade
Component
Function
KEGG
Process
F
row min
row max
NICM1(8A)
NICM1(8A)
NICM2(34A)
NICM2(34A)
NICM3(7A)
NICM3(7A)
NICM4(27A)
NICM4(27A)
ICM1(9A)
ICM1(9A)
ICM2(23A)
ICM2(23A)
ICM3(31A)
ICM3(31A)
ICM4(65A)
ICM4(65A)
Beta-2-glycoprotein 1
Collagen alpha-2(VI) chain
Collagen alpha-3(VI) chain (Fragment)
Collagen alpha-1(XIV) chain
Collagen alpha-1(VI) chain
Matrix metalloproteinase-9
Myosin light polypeptide 6
Myosin regulatory light polypeptide 9
Tropomyosin 3, isoform CRA_b
Myosin regulatory light chain 12A
Actin, cytoplasmic 1
Myosin-8
Myosin-11
Myosin-9
Plastin-2
T-complex protein 1 subunit beta
Cadherin-13
Endostatin (Fragment)
Filamin-A
Palladin
Vimentin
Calcium-binding mitochondrial carrier protein Aralar1
Actin, cytoplasmic 2, N-terminally processed
Myomesin-2
Myosin-13
Tubulin beta-3 chain
Cadherin-2
Voltage-dependent anion-selective channel protein 1
Voltage-dependent anion-selective channel protein 3
Methylcrotonoyl-CoA carboxylase beta chain, mitochondrial
Prohibitin
Voltage-dependent anion-selective channel protein 2
Angiotensinogen
NADH dehydrogenase [ubiquinone] 1 beta subcomplex subunit 5, mitochondria
Transitional endoplasmic reticulum ATPase
NADH dehydrogenase [ubiquinone] 1 alpha subcomplex subunit 2
Mitochondrial inner membrane protein
Endoplasmin
NADH dehydrogenase [ubiquinone] flavoprotein 2, mitochondrial
GTP:AMP phosphotransferase AK4, mitochondrial
Acyl-CoA-binding protein
NADH dehydrogenase [ubiquinone] 1 alpha subcomplex subunit 6
NADH dehydrogenase [ubiquinone] iron-sulfur protein 7, mitochondrial
G
4e-02 Thioester metabolic process
4e-02 Acyl-CoA metabolic process
3e-02 Citrate metabolic process
3e-02 Tricarboxylic acid cycle
2e-02 Lipid oxidation
2e-02 Fatty acid oxidation
4e-02 Fatty acid beta-oxidation
3e-02 Mitochondrial respiratory chain complex I assembly
3e-02 NADH dehydrogenase complex assembly
2e-02 Mitochondrial electron transport, NADH to ubiquinone
8e-04 Regulation of immune system process
8e-04 Positive regulation of immune system process
1e-03 Innate immune response
8e-04 Immune response
2e-03 Regulation of defense response
8e-04 Regulation of response to external stimulus
2e-03 Inflammatory response
8e-04 Regulation of inflammatory response
8e-04 Acute inflammatory response
3e-03 Protein maturation
3e-03 Protein activation cascade
6e-03 Adaptive immune response
8e-04 Response to wounding
8e-04 Wound healing
3e-03 Coagulation
8e-04 Import into cell
1e-03 Endocytosis
4e-03 Receptor-mediated endocytosis
6e-03 Phagocytosis
6e-03 Regulation of cell activation
NICM↑
ICM↑

Figure 4

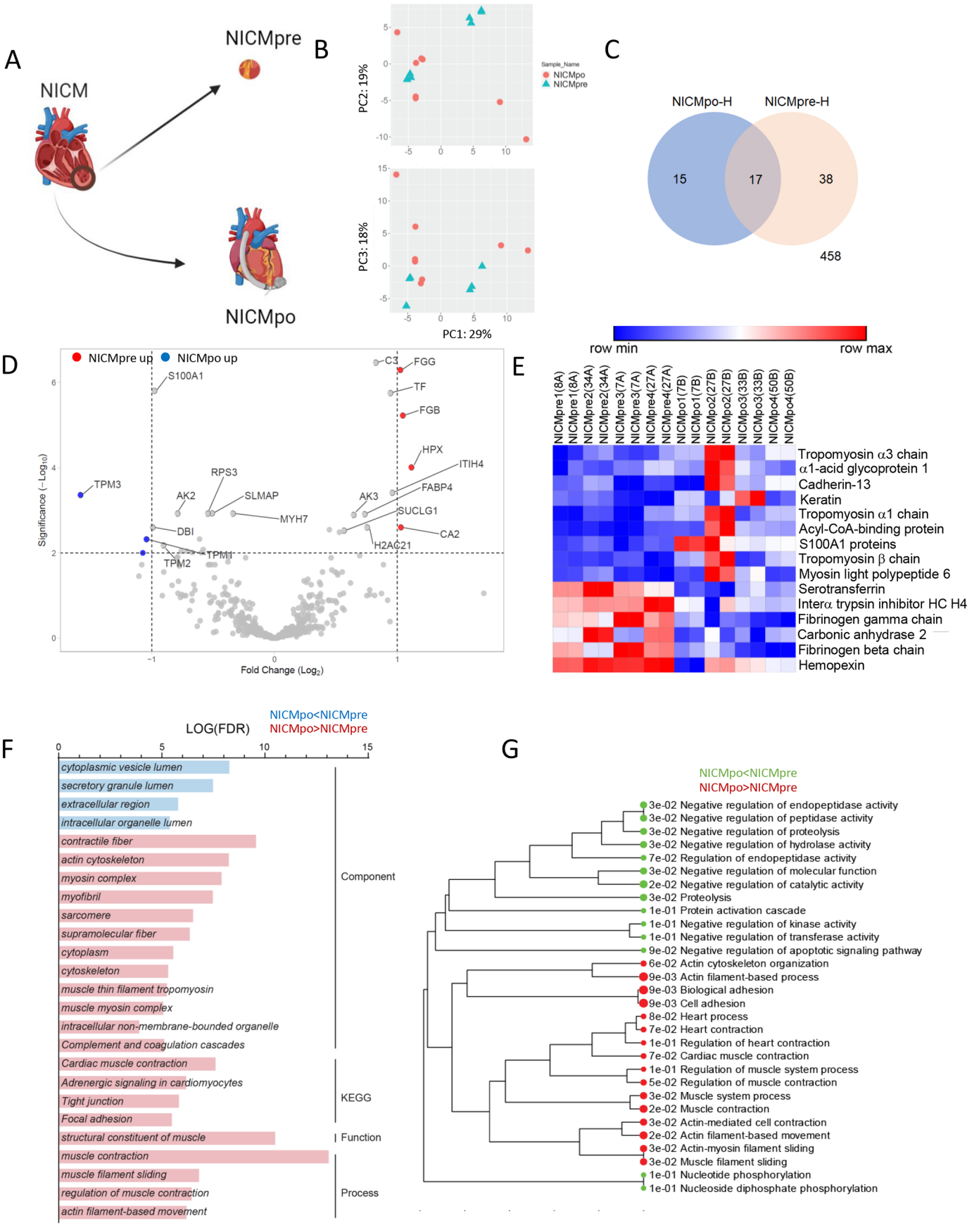
A
NICMpre
NICM
NICMpo
B
PC2: 19%
PC3: 18%
PC1: 29%
Sample_Name
NICMpo
NICMpre
C
NICMpo-H
NICMpre-H
15
17
38
458
D
NICMpre up
NICMpo up
S100A1
C3
FGG
TF
FGB
HPX
ITIH4
FABP4
TPM3
RPS3
AK2
SLMAP
MYH7
AK3
SUCLG1
CA2
DBI
TPM1
TPM2
H2AC21
Significance (−Log10)
Fold Change (Log2)
E
row min
row max
NICMpre1(8A)
NICMpre1(8A)
NICMpre2(34A)
NICMpre2(34A)
NICMpre3(7A)
NICMpre3(7A)
NICMpre4(27A)
NICMpre4(27A)
NICMpo1(7B)
NICMpo1(7B)
NICMpo2(27B)
NICMpo2(27B)
NICMpo3(33B)
NICMpo3(33B)
NICMpo4(50B)
NICMpo4(50B)
Tropomyosin α3 chain
α1-acid glycoprotein 1
Cadherin-13
Keratin
Tropomyosin α1 chain
Acyl-CoA-binding protein
S100A1 proteins
Tropomyosin β chain
Myosin light polypeptide 6
Serotransferrin
Interα trypsin inhibitor HC H4
Fibrinogen gamma chain
Carbonic anhydrase 2
Fibrinogen beta chain
Hemopexin
F
LOG(FDR)
NICMpo<NICMpre
NICMpo>NICMpre
cytoplasmic vesicle lumen
secretory granule lumen
extracellular region
intracellular organelle lumen
contractile fiber
actin cytoskeleton
myosin complex
myofibril
sarcomere
supramolecular fiber
cytoplasm
cytoskeleton
muscle thin filament tropomyosin
muscle myosin complex
intracellular non-membrane-bounded organelle
Complement and coagulation cascades
Cardiac muscle contraction
Adrenergic signaling in cardiomyocytes
Tight junction
Focal adhesion
structural constituent of muscle
muscle contraction
muscle filament sliding
regulation of muscle contraction
actin filament-based movement
Component
KEGG
Function
Process
G
NICMpo<NICMpre
NICMpo>NICMpre
3e-02 Negative regulation of endopeptidase activity
3e-02 Negative regulation of peptidase activity
3e-02 Negative regulation of proteolysis
3e-02 Negative regulation of hydrolase activity
7e-02 Regulation of endopeptidase activity
3e-02 Negative regulation of molecular function
2e-02 Negative regulation of catalytic activity
3e-02 Proteolysis
1e-01 Protein activation cascade
1e-01 Negative regulation of kinase activity
1e-01 Negative regulation of transferase activity
9e-02 Negative regulation of apoptotic signaling pathway
6e-02 Actin cytoskeleton organization
9e-03 Actin filament-based process
9e-03 Biological adhesion
9e-03 Cell adhesion
8e-02 Heart process
7e-02 Heart contraction
1e-01 Regulation of heart contraction
7e-02 Cardiac muscle contraction
1e-01 Regulation of muscle system process
5e-02 Regulation of muscle contraction
3e-02 Muscle system process
2e-02 Muscle contraction
3e-02 Actin-mediated cell contraction
2e-02 Actin filament-based movement
3e-02 Actin-myosin filament sliding
3e-02 Muscle filament sliding
1e-01 Nucleotide phosphorylation
1e-01 Nucleoside diphosphate phosphorylation

Figure 5


A
ICM
ICMpre
ICMpo
B
Principal component analysis (PCA)
PC2: 19% variance
PC1: 50% variance
Sample_Name
ICMpo
ICMpre
C
ICMpo-H
ICMpre-H
59
118
67
284
ICMpo up
ICMpre up
Significance (−Log10)
Fold Change (Log2)
TUBB3
KRT2
AGL
SELENBP1
POSTN
MYH4
RAN
ASPN
PCBD1
KRT1
ENO2
SDHA
CISD1
PCBP1
TUFM
NDUFB5
ACOT9
AK3
LRPPRC
HP
D
row min
row max
Haptoglobin
UPF0317 protein C14orf159, mitochondrial
Lipopolysaccharide-binding protein
PDZ and LIM domain protein 5
Apolipoprotein E
Cytochrome c1, heme protein, mitochondrial
Calreticulin
Protein-glutamine gamma-glutamyltransferase 2
Voltage-dependent anion-selective channel protein 1
Prothrombin
Ezrin
Elongation factor Tu, mitochondrial
Synemin
Beta-2-glycoprotein 1
40S ribosomal protein S3 (Fragment)
Cytochrome c oxidase subunit 5A, mitochondrial
Fibrinogen alpha chain
Myosin-10
1,4-alpha-glucan-branching enzyme
Histone-lysine N-methyltransferase SMYD1
14-3-3 protein gamma
Filamin-A
Heat shock protein beta-1
Cadherin-2
Succinyl-CoA ligase [ADP/GDP-forming] subunit alpha, mitochondrial
Heterogeneous nuclear ribonucleoproteins C1/C2
Actin, cytoplasmic 1
Protein disulfide-isomerase
Hydroxysteroid dehydrogenase-like protein 2
Myosin regulatory light chain 12A
Myosin-11
Ubiquitin carboxyl-terminal hydrolase 5
Cytochrome b-c1 complex subunit 9
Kininogen-1
Tropomyosin alpha-3 chain
Immunoglobulin lambda-like polypeptide 5
Ig kappa chain C region
Acylphosphatase-2
Stomatin-like protein 2, mitochondrial
Hemoglobin subunit beta
Collagen alpha-2(VI) chain
NADH dehydrogenase [ubiquinone] 1 alpha subcomplex subunit 2
NADH dehydrogenase [ubiquinone] flavoprotein 2, mitochondrial
Apolipoprotein A-I
Ig gamma-4 chain C region
Transthyretin
Collagen alpha-1(VI) chain
Basigin
Serotransferrin
Pigment epithelium-derived factor
Muscular LMNA-interacting protein
Acyl-CoA-binding protein
Protein S100-A1
Carbonic anhydrase 1
Antithrombin-III
Hemopexin
Ig gamma-1 chain C region
Serum albumin
Tropomyosin alpha-1 chain (Fragment)
Tubulin beta chain
Apolipoprotein A-IV
Adenylate kinase 2, mitochondrial
Collagen alpha-1(XIV) chain
Serum albumin (Fragment)
Collagen alpha-3(VI) chain (Fragment)
NADH dehydrogenase [ubiquinone] iron-sulfur protein 7, mitochondrial
Rab GDP dissociation inhibitor alpha
40S ribosomal protein SA
Alpha-2-HS-glycoprotein
Myosin-4
Ig lambda chain V-III region SH
Prolargin
E
LOG(FDR)
ICMpo<ICMpre
ICMpo>ICMpre
protein-containing complex binding
extracellular matrix
mitochondrion
mitochondrial membrane
mitochondrial protein complex
organelle envelope
cytoplasm
inner mitochondrial membrane protein complex
oxidoreductase complex
myelin sheath
protein-containing complex
organelle inner membrane
mitochondrial respiratory chain complex III
mitochondrial inner membrane
respiratory chain complex
mitochondrial respirasome
membrane protein complex
mitochondrial nucleoid
mitochondrial matrix
ATP metabolic process
purine ribonucleoside triphosphate metabolic process
purine ribonucleoside monophosphate metabolic process
purine ribonucleotide metabolic process
drug metabolic process
generation of precursor metabolites and energy
organophosphate metabolic process
oxidative phosphorylation
small molecule metabolic process
electron transport chain
oxidation-reduction process
cellular respiration
respiratory electron transport chain
Cardiac muscle contraction
Oxidative phosphorylation
Function
Component
Process
KEGG
F
ICMpo
ICMpre
2e-02 Positive regulation of protein phosphorylation
2e-02 Positive regulation of phosphorylation
2e-02 Positive regulation of protein modification process
2e-02 Positive regulation of phosphate metabolic process
2e-02 Positive regulation of phosphorus metabolic process
2e-02 Positive regulation of MAPK cascade
2e-02 ERK1 and ERK2 cascade
2e-02 Regulation of ERK1 and ERK2 cascade
2e-02 Negative regulation of apoptotic signaling pathway
2e-02 Regulation of reactive oxygen species metabolic process
2e-02 Regulation of defense response
2e-02 Regulation of response to external stimulus
2e-02 Activation of immune response
2e-02 Regulation of immune response
2e-02 Inflammatory response
2e-02 Acute inflammatory response
2e-02 Regulation of complement activation
2e-02 Regulation of acute inflammatory response
3e-02 Regulation of protein maturation
3e-02 Regulation of protein processing
9e-03 Protein processing
9e-03 Protein maturation
2e-02 Protein activation cascade
3e-02 Platelet activation
2e-02 Defense response to other organism
2e-02 Regulation of secretion
2e-02 Regulation of secretion by cell
3e-02 Regulation of cell activation
2e-02 Positive regulation of cell proliferation
2e-02 Skeletal system development

Figure 6